

Microdosimetry of radiation field from a therapeutic ^{12}C beam in water: a study with Geant4 toolkit

Lucas Burigo^{1,2,*}, Igor Pshenichnov^{1,3}, Igor Mishustin^{1,4} and Marcus Bleicher^{1,2}

¹ Frankfurt Institute for Advanced Studies, Johann Wolfgang Goethe University, 60438 Frankfurt am Main, Germany

² Institut für Theoretische Physik, Johann Wolfgang Goethe University, 60438 Frankfurt am Main, Germany

³ Institute for Nuclear Research, Russian Academy of Sciences, 117312 Moscow, Russia

⁴ Kurchatov Institute, Russian Research Center, 123182 Moscow, Russia

E-mail: burigo@fias.uni-frankfurt.de, pshenich@fias.uni-frankfurt.de

Abstract.

We model the responses of Tissue-Equivalent Proportional Counters (TEPC) to radiation fields of therapeutic ^{12}C beams in a water phantom and to quasi-monoenergetic neutrons in a PMMA phantom. Simulations are performed with the Monte Carlo model for Heavy Ion Therapy (MCHIT) based on the Geant4 toolkit. The shapes of the calculated lineal energy spectra agree well with measurements in both cases. The influence of fragmentation reactions on the TEPC response to a narrow pencil-like beam with its width smaller than the TEPC diameter is investigated by Monte Carlo modeling. It is found that total lineal energy spectra are not very sensitive to the choice of the nuclear fragmentation model used. The calculated frequency-mean lineal energy \bar{y}_f differs from the data on the axis of a therapeutic beam by less than 10% and by 10–20% at other TEPC positions. The validation of MCHIT with neutron beams gives us confidence in estimating the contributions to lineal energy spectra due to secondary neutrons produced in water by ^{12}C nuclei. As found, the neutron contribution at 10 cm distance from the beam axis amounts to $\sim 50\%$ close the entrance to the phantom and decreases to $\sim 25\%$ at the depth of the Bragg peak and beyond it. The presented results can help in evaluating biological out-of-field doses in carbon-ion therapy.

Keywords: theory and algorithms in physics of heavy-ion therapy, microdosimetry, Monte Carlo applications, simulation

PACS numbers: 87.53.Pb, 87.53.Rd, 87.53.Wz, 87.53.Vb

1. Introduction

At present time the heavy-ion therapy of cancer is one of the most advanced methods in radiation therapy (Scharadt et al. 2010, Elsaesser et al. 2010, Durante & Loeffler 2010). An elevated biological effectiveness of accelerated nuclei provides advantages in treatment of radioresistant solid tumors, but also requires a thorough treatment planning to reduce undesirable impact of radiation on healthy tissues. This should include, in particular, a realistic description of the production of secondary nuclear fragments. Such secondary particles deliver dose to the tissues located farther than the Bragg peak for primary nuclei and also around the primary beams.

Recently there were several experimental (Haettner et al. 2006) and theoretical (Gudowska et al. 2004, Böhlen et al. 2010, Pshenichnov et al. 2010) studies which confirmed the need to consider nuclear fragmentation reactions in heavy-ion therapy. In particular, as shown by measurements with a 400A MeV ^{12}C beam (with kinetic energy of 400 MeV per nucleon), about 70% of beam nuclei undergo fragmentation reactions (Haettner et al. 2006). Apart from the effect of primary beam attenuation, this means that the dose around the beam is delivered by light charged fragments, (e.g. protons and helium nuclei) and also by neutrons. In particular, neutrons may propagate large distances from their production points before they initiate secondary nuclear reactions.

As demonstrated by studies with various transport codes, such as SHIELD-HIT (Gudowska et al. 2004), FLUKA and Geant4 (Böhlen et al. 2010, Pshenichnov et al. 2010), the measured attenuation of the primary carbon beam and production of heavier fragments are generally well reproduced by the theory. However, as follows from the same studies, there are problems with quantitative description of the yields, angular distributions and energy spectra for several kinds of fragments produced in fragmentation reactions in water. In particular, the yields of alpha-particles are underestimated. This may be related to neglecting the cluster structure of light nuclei, which leads to the underestimation of decays of excited nuclei into channels containing alphas. It is unlikely that such deficiency will be eliminated soon, as this will require combining dynamical and statistical models of nuclear reactions with sophisticated nuclear structure models into a unified, but still computationally effective tool.

Nuclear fragmentation models calculate the yields of secondary fragments as functions of their charges and velocities. However, the impact of specific particle species on living cells is rather correlated with their linear energy transfer (LET) values. The LETs of particles with different charges Z , but similar velocities in first approximation are proportional to their Z^2 . At the same time ions of different velocities and charges may have similar LET (Guetersloh et al. 2004). Therefore, the reliability of nuclear fragmentation models, in particular used in Geant4 calculations (Böhlen et al. 2010, Pshenichnov et al. 2010), should be also evaluated with respect to calculations of LET or related quantities.

The biological action of radiation is commonly characterized by microdosimetric

quantities (International Commission of Radiation Units and Measurements (ICRU) 1983, Rossi 1990, Lindborg & Nikjoo 2011) such as lineal energy y , its probability density $f(y)$ and dose probability density $d(y)$. Frequency-mean, \bar{y}_f , and dose-mean, \bar{y}_d , lineal energies are defined as the first moments of the corresponding distributions, see section 2 for their definitions. These distributions are routinely measured by means of Tissue Equivalent Proportional Counters (TEPC) (Waker 1995, Waker 2006).

In a complex radiation field different particles can eventually contribute with similar y . Therefore, the resulting y -distribution is build as the sum of contributions from primary and all secondary particles passing TEPC. Measurements and calculations of microdosimetric quantities related to heavy-ion therapy were reported by several authors. In particular, microdosimetric quantities were used to characterize the biological dose from therapeutic ^{12}C beams (Kase et al. 2006, Kase et al. 2011, Martino et al. 2010). Similar measurements were performed for the first time for ^7Li beams (Martino et al. 2010). Simulations with the PHITS code were done for a wall-less TEPC (Tsuda et al. 2010). The energy deposition inside and around ^7Li and ^{12}C beams in water were calculated with SHIELD-HIT and FLUKA codes (Hultqvist et al. 2010, Taleei et al. 2011), but without implementing the exact geometry of the TEPC detector and, respectively, without calculating y -distributions. The FLUKA code was also used to simulate responses of TEPC to various ions (Böhlen et al. 2011), including y -distributions for TEPCs located on the beam axis inside a water phantom irradiated by ^{12}C beam (Böhlen et al. 2012).

In our previous papers (Pshenichnov et al. 2005, Pshenichnov et al. 2006, Pshenichnov et al. 2007, Pshenichnov et al. 2008, Pshenichnov et al. 2010, Mishustin et al. 2010) we validated the Geant4 toolkit (Agostinelli et al. 2003, Allison et al. 2006) for use in heavy-ion therapy simulations. The depth-dose distributions (Pshenichnov et al. 2006) and production of positron-emitting nuclei (Pshenichnov et al. 2007, Pshenichnov et al. 2008) were calculated by means of the Monte Carlo model for Heavy Ion Therapy (MCHIT) based on Geant4. Special effort was made to evaluate the quality of nuclear fragmentation models (Pshenichnov et al. 2010, Mishustin et al. 2010) by comparing theoretical predictions with experimental data on fragment yields (Haettner et al. 2006).

The main purpose of the present work consists in accurate modeling of in-field and out-of-field microdosimetry spectra, their averages and contributions from secondary neutrons for pencil-like ^{12}C beams, which are typical for facilities with scanned therapeutic beams. In this case a TEPC placed in a water phantom is impacted by a complex radiation field. It is either irradiated by a mixture of beam nuclei and secondary fragments or exposed exclusively to such fragments far from beam axis or beyond the Bragg peak.

In order to achieve the main goal of our study the following specific issues are investigated:

- the sensitivity of calculational results to the choice of the Geant4 models and their parameters for nuclear reactions and production and transport of secondary

- electrons, e.g. to the production thresholds;
- the accuracy of the MCHIT model in describing microdosimetry spectra of quasi-monoenergetic neutrons as a prerequisite for estimating the contribution of secondary neutrons from ^{12}C beam;
 - the level of distortion of microdosimetry variables due to the impact of a focused ^{12}C beam with its width smaller than the TEPC diameter, i.e. when the condition of random crossing of TEPC by particles is violated or several nuclei of fragments traverse the TEPC in a single event;
 - the dose per beam particle at various points inside the water phantom and the distortion of the dose field measured with TEPC due to its finite size and gradients of radiation field;
 - the correspondence between calculated and measured \bar{y}_f and LET of beam particles for various beam profiles and media surrounding TEPC.

2. Basics of microdosimetry method and relevant measurements

It is known that the impact of charged particles on eukaryotic cells is defined not only by the energy imparted to the cell volume (i.e. by the absorbed dose), but also by the total number and spatial correlations of local energy deposits to DNA molecules inside the cell nucleus. Such deposits lead to spatially distributed DNA lesions caused mainly by free electrons which surround a track of a charged particle. The pattern of stochastic impacts on DNA resulting in single, double or more complex breaks of DNA strands essentially depends on the projectile charge, mass and velocity. It is defined by the number of electrons per unit of the track length as well as on their energies. All these characteristics differ for photon, electron, proton and nuclear beams. In particular, carbon nuclei successfully used for particle therapy of cancer are characterized by elevated biological effectiveness in the Bragg peak region as compared to photons and protons (Elsaesser et al. 2010, Durante & Loeffler 2010). Thus, these biological effects of ion beams should be taken into account while developing the treatment planning systems used in particle therapy (Kase et al. 2006, Kraemer & Durante 2010, Kase et al. 2011).

Since DNA molecules are typically confined inside cell nuclei, which are structures of a few-micrometer size, it is desirable to study energy deposition patterns at the micrometer scale. In particular, the in-beam microscopy is used in experiments on irradiation of living cells. With this tool, the tracks of charged particles can be well explored, if visualized by biological markers for DNA damage (Tobias et al. 2010).

Since many years measurements with Tissue-Equivalent Proportional Counters (TEPC) (International Commission of Radiation Units and Measurements (ICRU) 1983) are considered as a practical tool for studying patterns of energy deposition to micrometer-size objects by various kinds of radiation. The TEPC considered in this paper has a chamber with an inner diameter of 12.7 mm filled with low-pressure tissue-equivalent (TE) gas (Martino et al. 2010). It emulates a tissue-equivalent

region of a micrometer size. In this way the energy deposited to the sensitive gas volume of this device can be related to the energy that would be deposited to a cell nucleus (International Commission of Radiation Units and Measurements (ICRU) 1983). As demonstrated by several authors, see e.g. (Rossi 1990, Lindborg & Nikjoo 2011), microdosimetric variables are directly related to the radiation quality factor used to quantify risks from various kinds of radiation.

Due to the stochastic nature of particle transport in media, the amount of energy ϵ delivered to a sensitive volume representing a cell nucleus changes from one event to another. The value of ϵ in each energy deposition event can be measured by a TEPC (Waker 1995, Waker 2006, Lindborg & Nikjoo 2011), as the measured electronic signal is expected to be proportional to ϵ . This technique allows one to obtain the probability distributions for lineal energy $y = \epsilon/\bar{l}$, where \bar{l} is the mean chord length of the sensitive volume used as a detector. If one assumes that particles representing a homogeneous radiation field traverse a spherical detector randomly at various impact parameters, then $\bar{l} = 2/3d$.

There were several experimental (Guetersloh et al. 2004, Taddei et al. 2006) and theoretical (Nikjoo et al. 2002, Taddei et al. 2008) studies of TEPC responses to heavy-ions. In these measurements and calculations the dependence of ϵ on the impact parameter of the ion track was investigated in detail. As demonstrated by Taddei and co-authors (Taddei et al. 2008), calculations based on the Geant4 toolkit can successfully reproduce the performance of a TEPC (Far West Technology Inc., model LET-1/2) irradiated by ^4He , ^{12}C , ^{16}O , ^{28}Si and ^{56}Fe nuclei.

Since lineal energy y varies from one event to another, the frequency-mean lineal energy \bar{y}_f , which characterizes the probability density $f(y)$, can be introduced (International Commission of Radiation Units and Measurements (ICRU) 1983):

$$\bar{y}_f = \int_0^\infty y f(y) dy . \quad (1)$$

The value of \bar{y}_f is the first moment of $f(y)$ and serves as a measurable approximation for LET.

In the following also $yd(y)$ -distributions, with $d(y) \equiv yf(y)/\bar{y}_f$ defined as the dose probability density, will be considered. The dose-mean lineal energy \bar{y}_d is calculated as the second moment of the $f(y)$ -distribution divided by its first moment:

$$\bar{y}_d = \int_0^\infty y d(y) dy = \frac{1}{\bar{y}_f} \int_0^\infty y^2 f(y) dy . \quad (2)$$

The value of \bar{y}_d is related to the quality of radiation.

For a spherical sensitive volume filled with gas the total dose D is given by a useful formula (International Commission of Radiation Units and Measurements (ICRU) 1983):

$$D = \frac{0.204}{d^2} \bar{y}_f . \quad (3)$$

Here d corresponds to the diameter of the sensitive volume expressed in μm , \bar{y}_f in $\text{keV}/\mu\text{m}$ and D is obtained in Gy.

Due to its compactness the TEPC device can be located at various positions inside and outside of phantoms irradiated by therapeutic beams. The microdosimetry measurements with a monoenergetic 400A MeV ^{12}C beam (Endo et al. 2005) were made together with the identification of charges of secondary fragments by scintillation counters by the time-of-flight (TOF) method. In this way the above-described microdosimetry technique supplements the measurements of fragment yields by particle identification made outside the phantom with more bulky detectors, see e.g. (Haettner et al. 2006).

Further measurements were performed with phantoms irradiated by 290A MeV ^{12}C beam with a traditional walled TEPC (Endo, Takada, Onizuka, Tanaka, Maeda, Ishikawa, Miyahara, Hayabuchi, Shizuma & Hoshi 2007), also with fragment charge identification, and later (Tsuda et al. 2010) with a wall-less counter without tagging fragments. Recently the results of microdosimetry measurements with 290A MeV Spread Out Bragg Peak (SOBP) carbon-ion beam were also reported (Endo et al. 2010, Kase et al. 2011). In all these measurements the TEPCs were located at the beam axis.

Microdosimetry measurements on the beam axis as well as off-axis in a water phantom irradiated by a pencil-like ^{12}C beam were performed at GSI (Martino et al. 2010). Similar studies at carbon-ion and proton radiotherapy facilities with passive beam delivery were also performed at TEPC positions outside the treatment field (Yonai et al. 2010). The collected microdosimetry data challenge the theoretical methods aimed to describe particle transport in tissue-like media.

3. Physics models used in MCHIT simulations

For the purposes of the present study we further developed our Monte Carlo model for Heavy-Ion Therapy (MCHIT) (Pshenichnov et al. 2006, Pshenichnov et al. 2007, Pshenichnov et al. 2008, Pshenichnov et al. 2010, Mishustin et al. 2010) to simulate microdosimetry measurements with TEPC devices. The model is currently based on the Geant4 toolkit (Agostinelli et al. 2003, Allison et al. 2006) of version 9.4 with patch 02. Input parameters for a MCHIT run are provided via a set of user interface commands which define the beam particle, the energy distribution of the beam, its spot size, angular divergence, as well as the dimensions and composition of the phantom used in a particular experimental set-up.

A detailed description of the physics models included in the Geant4 toolkit is given in the Geant4 Physics Reference Manual (*Geant4 Physics Reference Manual* 2011). A set of models which are relevant to a particular simulation problem should be activated by the application developer. Such models are usually grouped in a physics list. In order to involve certain models into simulation, one can either use the so-called predefined physics lists, or implement customized physics lists, or even use a combination of these two options. The predefined physics lists are provided by Geant4 developers and distributed along with the Geant4 source code. It is convenient to use separate physics lists for electromagnetic and hadronic physics.

3.1. Electromagnetic physics

The electromagnetic processes are described by means of several predefined physics lists of Geant4. The physics list called “Standard Electromagnetic Physics Option 3” is recommended by the Geant4 developers for simulations related to particle therapy. As demonstrated (Lechner et al. 2010), the measured positions of the Bragg peak for carbon nuclei of various energies in water are well reproduced with this physics list. The involved physics models simulate the energy loss and straggling of primary and secondary charged particles due to interaction with atomic electrons. The multiple Coulomb scattering of charged particles on atomic nuclei is also simulated.

At each simulation step the ionization energy loss of a charged particle is calculated according to the Bethe-Bloch formula or interpolated between values listed in a table, depending on the particle type and energy (*Geant4 Physics Reference Manual* 2011). In particular, the Bethe-Bloch formula with the shell, density and high-order corrections is applied in *G4BetheBlochModel* to protons with kinetic energy above 2 MeV. Below 2 MeV the stopping power parameterizations (International Commission of Radiation Units and Measurements (ICRU) 1993) are used for protons in *G4BraggModel*. The same methods are applied to alpha particles taking into account the corresponding mass scaling with respect to proton. An interpolation of stopping power tables (International Commission of Radiation Units and Measurements (ICRU) 2005) is implemented in *G4IonParametrisedLossModel* to calculate electromagnetic energy loss of ions heavier than helium with energies relevant to our study, below 1000 MeV. The lowest kinetic energy for the production of δ -electrons in this standard physics list is 990 eV. The emission of δ -electrons with energies below 990 eV is not simulated, but their energies are attributed to the local energy deposition. Another predefined physics list, which extends the capability of electromagnetic models to produce and transport δ -electrons down to 100 eV, namely *G4EmPenelope* based on the Penelope model (*Geant4 Physics Reference Manual* 2011), was also used for investigation of the impact of this energy threshold for the production of secondary electrons.

In order to reduce the CPU time without affecting the accuracy of calculations, different cuts for production of electrons were applied in different materials. They are listed in table 1.

The cut in range for TE gas was defined by the lowest energy of electrons which can be transported by the correspond models. This limitation in the electromagnetic models amounts for a cut in range of 9 mm for the standard electromagnetic models and 3 mm for the Penelope models. Since 9 mm is of the same order as the diameter of the sensitive volume, the comparison of results between the standard and Penelope models helps to understand how this limitation undermines the results.

In a 1.27 mm-thin plastic shell of the TEPC detector the cut in range for electrons was reduced to 10 μm . This helps to simulate accurately grazing interactions of particles with the plastic shell, as secondary particles produced in plastic can propagate further into gas. According to the default settings of Geant4 there were no cuts for secondary

Table 1. Cut in range and energy production threshold for electrons in the phantom and TEPC materials applied in MCHIT simulations with Standard Electromagnetic Physics (Option 3) and with the Penelope model.

material	Standard opt 3		Penelope	
	cut in range (mm)	energy threshold (keV)	cut in range (mm)	energy threshold (keV)
water	0.1	85.	0.1	85.
A-150 TE plastic (1.27 mm)	0.01	17.6	0.001	0.3
TE gas (12 kPa)	9	0.99	3	0.1

nucleons and nuclear fragments, and all produced particles (including electrons) after their production are transported down to zero kinetic energy.

3.2. Modeling nuclear fragmentation

A customized physics list was implemented for the description of hadronic processes. Modifications in this physics list with respect to our previous publications concern the modeling of inelastic nucleus-nucleus interactions. In the present study we considered two Geant4 models to describe the first stage of nucleus-nucleus collisions, namely, the Light Ion Binary Cascade (G4BIC) and the Quantum Molecular Dynamics (G4QMD) models. In our earlier publication (Pshenichnov et al. 2010) the G4BIC and G4 abrasion models were employed to describe such reactions. Recent improvements in the G4QMD code (Koi 2010), as well as the conclusions based on the comparison of G4BIC and G4QMD (Böhlen et al. 2010), suggest that the G4QMD model can be also successfully used for modeling nuclear fragmentation of carbon nuclei. Therefore, in our calculations of microdosimetric distributions both options to simulate nuclear fragmentation, G4BIC and G4QMD, were used.

Excited nuclear fragments are frequently produced in addition to free nucleons as a result of simulation of a nucleus-nucleus collision event by the G4BIC and G4QMD models. Therefore, the G4ExcitationHandler of Geant4 is used to simulate subsequent decays of excited nuclear fragments by applying various de-excitation models depending on the mass and excitation energy of these fragments.

The Fermi break-up model (G4FermiBreakUp) is applied to nuclei lighter than fluorine. It is designed to describe explosive disintegration of excited light nuclei (Bondorf et al. 1995) and it is highly relevant to collisions of light nuclei with nuclei of tissue-like materials. As demonstrated (Mishustin et al. 2010) G4BIC linked with G4FermiBreakUp better describes the production of lithium and beryllium nuclei, as well as secondary neutrons by ^{12}C nuclei in water and PMMA compared to the option of G4BIC linked with the nuclear evaporation model. As demonstrated by Böhlen et al. (Böhlen et al. 2010) the combination of G4QMD and G4FermiBreakUp also describes

data well. Therefore, we used G4FermiBreakUp to de-excite light fragments also in the present work.

3.3. Hits and deposited energy

We use the primitive scorer classes of Geant4 to calculate physical quantities which characterize the TEPC response in each event. The energy ϵ deposited to the TEPC sensitive volume is calculated by means of the *G4PSEnergyDeposit* scorer. This scorer stores a sum of particles' energy deposits to the sensitive volume in each event. The number of tracks N that pass through the TEPC sensitive volume, but do not start or stop inside it, is calculated by employing *G4PSPassageCellCurrent*. In particular, this means that numerous low-energy δ -electrons which are produced by energetic nuclei and stopped inside the TE gas are not counted by this scorer. Finally, *G4PSPassageTrackLength* is used to calculate the total track length l inside the TEPC sensitive volume in single and multi-particle events. With this scorer the track length is defined as the sum of step lengths of the particles inside the volume, and again only tracks which traverse the volume are taken into account. This means that newly-generated or stopped tracks inside the volume are excluded from the calculation of l . The employed *G4PSPassageTrackLength* scorer is thus insensitive to those secondary electrons which were produced by a fast particle inside the TEPC sensitive volume, but stopped inside it. The total track length is scored in order to evaluate the mean track length through the detector for comparison with the mean chord length $\bar{l} = 2/3d$ in the standard conditions for microdosimetry measurements.

4. Modeling experimental set-up

In this work we calculate microdosimetric distributions and compare them with results of two experiments (Nakane & Sakamoto 2001, Martino et al. 2010). In the first experiment a PMMA phantom was irradiated by broad quasi-monoenergetic neutron beams at the Japan Atomic Energy Research Institute (JAERI). In the second experiment a water phantom was irradiated by carbon and lithium pencil-like beams at GSI. The same type of TEPC device (Far West Technology Inc., model LET-1/2) was used by both groups. This allowed us to validate our calculational approach for this specific TEPC model first with neutron irradiation data (Nakane & Sakamoto 2001), and then extend it to the GSI measurements (Martino et al. 2010) with ^{12}C beam. In a previous study (Mishustin et al. 2010) we demonstrated that MCHIT can estimate reasonable well the energy and angular spectra of secondary neutrons produced by 200A MeV carbon beam in thick water target. Therefore, if MCHIT is able to reproduce microdosimetry spectra for neutrons measured with a TEPC we believe that the contribution of secondary neutrons to the microdosimetry spectra for carbon beam measured with the same TEPC device can be estimated with confidence.

The actual TEPC dimensions and the chemical composition of TEPC materials

were implemented as accurate as possible in our simulations. It was assumed that the tissue equivalent gas was propane C_3H_8 (55%) with addition of CO_2 (39.6%) and N_2 (5.4%). A gas container was defined in simulations as a shell of tissue-equivalent plastic composed of H (10.1%), C (77.6%), N (3.5%), O (5.2%), F (1.7%) and Ca (1.9%), in accordance with the properties of the NIST material Shonka A-150 plastic. An aluminum outer shell of the TEPC was also introduced, although simulation results were found to be rather insensitive to the presence of the Al shell because of its small thickness. The central wire located inside the gas sphere was not considered in the simulations. Following Taddei et al. (Taddei et al. 2006), it was assumed that quite rare events in which a projectile particle interacted with this wire are rejected in measurements. We also neglect the bending of the simulated tracks due to the voltage applied to the TEPC.

Experimental results for a TEPC located at 5 cm depth inside the PMMA phantom irradiated by 40 MeV and 65 MeV quasi-monoenergetic neutrons were selected from JAERI data to validate the MCHIT model. The pressure of the tissue equivalent gas was 9.03 kPa which emulated a tissue sphere of $2.07 \mu\text{m}$ in diameter.

In the second experiment (Martino et al. 2010) a water phantom of $30 \times 30 \times 30 \text{ cm}^3$ (including side walls made of PMMA) was irradiated by a 300A MeV ^{12}C beam. In the simulations the parameters of the ^{12}C beam used at GSI were implemented as accurate as possible. The beam had a concentric spot with a size of 3 mm FWHM at beam exit window, an angular distribution with the Gaussian profile of 1 mrad FWHM, and an energy distribution with the Gaussian profile of 0.2% FWHM. The $yd(y)$ -distributions per beam particle measured at nine points inside the water phantom were reported (Martino et al. 2010). They correspond to 0 cm, 2 cm and 10 cm radii and to three values of depth: at the plateau of the depth-dose curve, at the Bragg peak and in the tail region. In this experiment water was enclosed in a container with a 20 mm thick PMMA wall. Carbon nuclei also penetrated through a vacuum window made of aluminum, a scintillation detector and a parallel-plate ion chamber installed in front of the phantom. These beam-line elements and PMMA walls of the phantom were estimated by Martino et al. as equivalent water thickness of 25.1 mm. This thickness was applied to the TEPC depth in order to compare the data with simulation results, since calculations were performed with an equivalent wall-less water phantom of $30 \times 30 \times 30 \text{ cm}^3$. It was found that a 2 mm shift to a deeper position of the TEPC is required in order to reproduce the peak in the $yd(y)$ spectrum for the TEPC positioned in the vicinity of the Bragg peak on the beam axis as well as the depth-dose profile. At this position the microdosimetry spectrum is highly sensitive to a few millimeters shift of the device. One can attribute this shift to uncertainties in the measurements of TEPC positions, beam energy and the equivalent water thickness in front of the water phantom. Some inaccuracy of the electromagnetic physics models of Geant4 can not be excluded as well. For consistency this shift was applied to all TEPC positions as a systematic correction. The gas pressure was set to the experimental value of 12 kPa which corresponds to a sphere of tissue of $2.75 \mu\text{m}$ in diameter. The TEPC positions

used in our simulations are listed in table 2.

Using the axial symmetry of the set-up in the second experiment we replaced a single physical TEPC by a ring of identical virtual TEPCs located at the same depth and radial distance from the beam axis. During each run the lineal energy events were scored in a histogram corresponding to a particular ring. At the end of the run the number of events in each lineal energy bin were divided by the number of virtual counters in the ring and thus became equivalent to a single physical counter. With this method one can increase the simulated number of hits for those positions of counters where hits are scarce. This is particularly important for TEPCs located at large distances, e.g., at 10 cm, from the beam axis. The number of counters in each ring and the positions of the rings with respect to the beam axis were chosen to avoid any crosstalk impacts on the virtual detectors. This was done to satisfy the condition that the particles produced inside one of the virtual counters, or which have just traversed it, should not hit other counters. Therefore, calculations for the nine TEPC positions listed in table 2 were split into three independent runs. During the run ‘‘I’’ three outer rings of TEPCs of 10 cm in radius each consisting of 24 counters were placed in the water phantom. In the same run a counter on the beam axis and a ring of 2 cm in radius consisting of four TEPCs were placed at 27.71 cm depth. Each of the runs ‘‘II’’ and ‘‘III’’ was executed with a ring of 2 cm in radius consisting of four counters and with a single counter located at the same depth in the center of the ring. Typically, the histories of 10^7 to 5×10^7 ^{12}C nuclei traversing the phantom were simulated in each run.

Table 2. Positions of the TEPC counters inside the water phantom used in MCHIT simulations and their labeling in the following text and figures. TEPCs were grouped into rings with a number of counters in each ring depending on the ring radius. Each TEPC position was modeled in a certain run labeled in the last column.

radius (mm)	depth (mm)	TEPC’s position notation	number of counters in the ring	run label
0.	52.1	0 cm, plateau	1	III
0.	179.1	0 cm, peak	1	II
0.	277.1	0 cm, tail	1	I
20.	52.1	2 cm, plateau	4	III
20.	179.1	2 cm, peak	4	II
20.	277.1	2 cm, tail	4	I
100.	52.1	10 cm, plateau	24	I
100.	179.1	10 cm, peak	24	I
100.	277.1	10 cm, tail	24	I

5. TEPC response to quasi-monoenergetic neutron beams

It is expected that radiation fields far from the beam axis have a large contribution from neutrons produced in fragmentation of beam nuclei. Therefore, before performing

microdosimetry simulations with nuclear beams we checked the validity of the MCHIT model with respect to irradiation of the same TEPC model by neutrons. The data obtained with quasi-monoenergetic neutron beams (Nakane & Sakamoto 2001) were used for this purpose. Energy spectra of neutrons used in the two sets of measurements (Nakane & Sakamoto 2001) were modeled as superpositions of Gaussian peaks centered at 40 and 65 MeV, respectively, and broad plateaus. The ratios between the flux of neutrons with energies within the peak and the total neutron flux were set to 1:2.768 and 1:2.807 for 40 and 65 MeV spectra, respectively, following the estimations by Nakane et al. (Nakane & Sakamoto 2001). As proved by our simulations, the calculated $yd(y)$ distributions are not very sensitive to these ratios. For example, the calculations with these ratios set to 1:3.5 provide results similar to ones obtained with original ratios (Nakane & Sakamoto 2001). In the following the above-described spectra composed of peaks and plateaus are referred to as “40 MeV” and “65 MeV” neutrons.

MCHIT results for a TEPC located at 5 cm depth inside a PMMA phantom of $30 \times 30 \times 30 \text{ cm}^3$ are shown in figure 1 together with the experimental data (Nakane & Sakamoto 2001). In this experiment the phantom was irradiated by “40 MeV” neutrons, and the TEPC was located on the axis of the irradiation field. Neutrons were delivered to the phantom via a collimator of 10.9 cm in diameter, which was much larger than the diameter of the TEPC. Since neutrons traversed the TEPC randomly at various impact parameters, the mean neutron path \bar{l} inside the TEPC sensitive volume amounted to $2/3$ of its diameter. As explained in section 2, this corresponds to the standard conditions of microdosimetry measurements (International Commission of Radiation Units and Measurements (ICRU) 1983).

The results presented in figure 1 were obtained by simulating 4×10^8 primary neutrons for each of the runs where either G4QMD or G4BIC were used to simulate neutron-induced nuclear reactions. The number of primary particles was such that the fluctuations in the histogram is of the same order as those presented by the experimental data. No error bars are presented due to the lack of error bars in the reported experimental values. The microdosimetry parameters computed from the spectra are $\bar{y}_f = 7.54 \text{ keV}/\mu\text{m}$ ($\bar{y}_d = 84.2 \text{ keV}/\mu\text{m}$) for the experiment and $7.55 \text{ keV}/\mu\text{m}$ ($110 \text{ keV}/\mu\text{m}$) and $6.21 \text{ keV}/\mu\text{m}$ ($80.2 \text{ keV}/\mu\text{m}$) for the simulations with G4BIC and G4QMD, respectively. Microdosimetry spectra calculated for the same set-up, but for the irradiation with “65 MeV” neutrons are shown separately in figures 2 and 3. The corresponding microdosimetry parameters are $\bar{y}_f = 5.51 \text{ keV}/\mu\text{m}$ ($\bar{y}_d = 75.2 \text{ keV}/\mu\text{m}$) for the experiment and $5.33 \text{ keV}/\mu\text{m}$ ($86.1 \text{ keV}/\mu\text{m}$) and $4.75 \text{ keV}/\mu\text{m}$ ($84.2 \text{ keV}/\mu\text{m}$) for the simulations with G4BIC and G4QMD, respectively.

Neutrons do not transfer their energy directly to the TEPC gas volume, but rather through secondary charged particles produced in neutron interactions with nuclei in the gas cavity, TEPC wall or even in surrounding layers of PMMA. Several recoil particles can be produced by a single neutron. MCHIT makes it possible to estimate partial contributions from each kind of recoil particles to the total $yd(y)$ curve. Such contributions were calculated as following. Firstly, the amount of energy deposited to

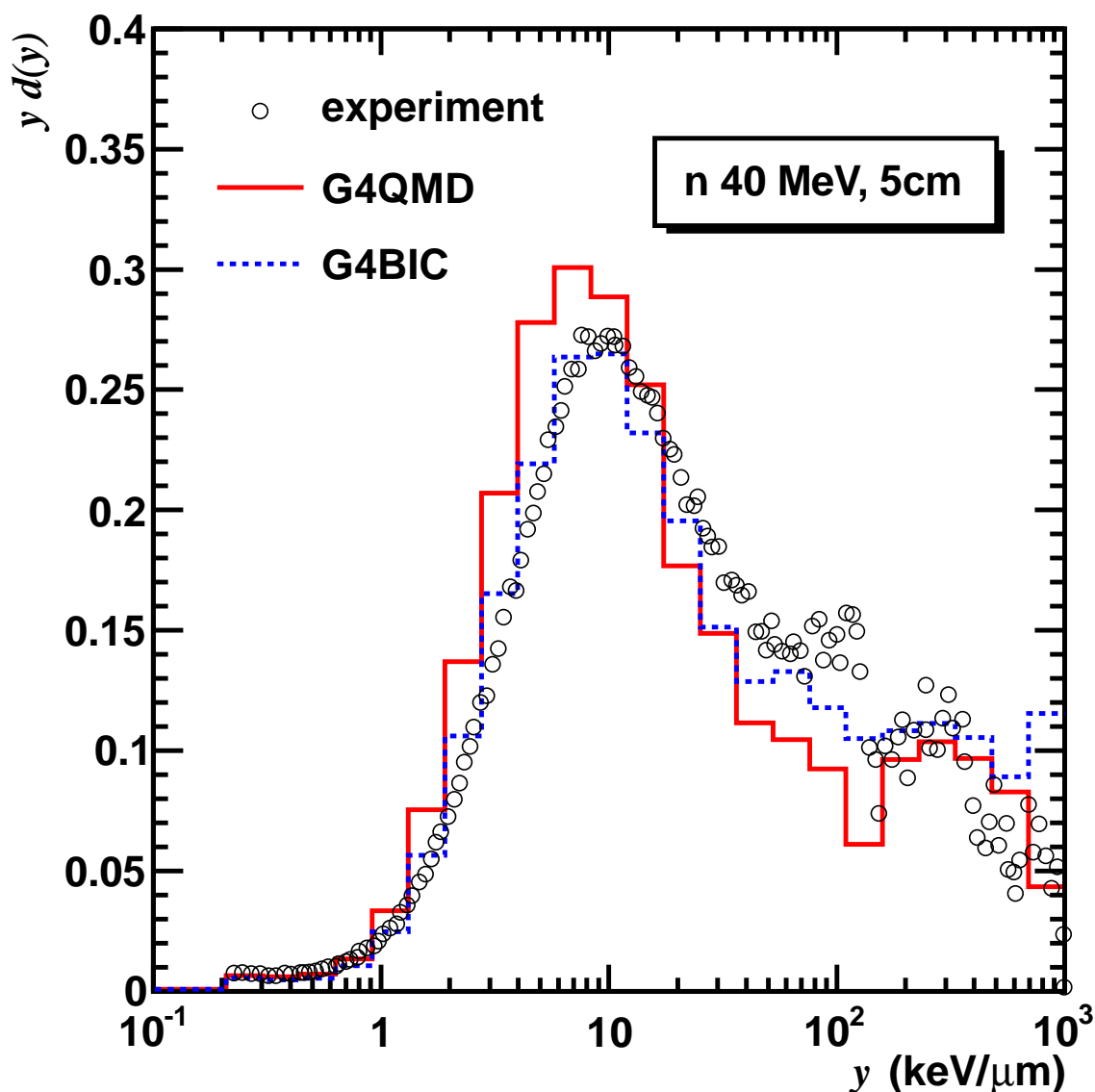


Figure 1. Calculated microdosimetric spectra for a TEPC at 5 cm depth inside a PMMA phantom irradiated by quasi-monoenergetic “40 MeV” neutrons. Theoretical results obtained with G4QMD and G4BIC models are presented by solid and dashed histograms, respectively. Experimental data (Nakane & Sakamoto 2001) are shown by points.

the sensitive volume by every kind of particle is scored separately at each lineal energy event. Secondly, the relative contribution to $yd(y)$ for each kind of particle in this event is calculated from the ratio between the energy deposited by particles of a given kind and the total energy deposited in the event. The partial contributions from specific particles to $yd(y)$ for the whole run are shown in figures 2 and 3.

Contributions of specific secondary particles to the $yd(y)$ distribution for “65 MeV” neutrons are shown in figure 2. These distributions were obtained with G4BIC applied to simulate neutron-induced nuclear reactions. This figure demonstrates the origins of a

peak at $y \sim 7 \text{ keV}/\mu\text{m}$ and a shoulder extending to higher y values. The peak is due to recoil protons, while the shoulder is formed by more heavy recoil nuclei, mostly by alpha-particles ($y > 30 \text{ keV}/\mu\text{m}$) and carbon nuclei ($y > 100 \text{ keV}/\mu\text{m}$). The contributions from boron, lithium and beryllium nuclei are much smaller and attributed mostly to $y > 200 \text{ keV}/\mu\text{m}$. The microdosimetric distributions for “40 MeV” neutrons (not shown) were calculated in a similar way. In this case the maximum is located at $y \sim 9 \text{ keV}/\mu\text{m}$ due to less energetic primary neutrons. Therefore, neutrons transfer less energy to recoil protons, which get slower and therefore have higher LET values.

Contributions of various recoil particles to $yd(y)$ distribution calculated with G4QMD for “65 MeV” neutrons are shown in figure 3. As seen from the figure, MCHIT predicts more fast recoil protons (with lower LET) compared to experimental data. This leads to a shift of the peak of the calculated distribution to lower y . Regarding recoil nuclei, results obtained with G4QMD model differ from measurements at $y \sim 100 \text{ keV}/\mu\text{m}$ where energy deposition events are mostly caused by helium nuclei. This can be explained by an underestimation of alpha-particle yields in neutron-induced reactions simulated by this model.

As shown in this section, the MCHIT model with G4BIC applied to simulate neutron-induced reactions demonstrates a better agreement with experimental data compared to the MCHIT with G4QMD. The maximum of the theoretical $yd(y)$ distributions calculated with G4QMD is slightly shifted to lower y values with respect to the measurements (Nakane & Sakamoto 2001). The proton edge at $y \sim 100 \text{ keV}/\mu\text{m}$ is better reproduced by G4BIC. The measured \bar{y}_f is well reproduced by G4BIC, but \bar{y}_d is overestimated for “40 MeV” neutrons due to a higher probability of large size events. G4QMD underestimates the frequency-mean lineal energy by 14–18% but better reproduces the dose-mean lineal energy compared to G4BIC. Nonetheless, the overall shape of the microdosimetry spectra and the magnitude of microdosimetry parameters for quasi-monoenergetic neutrons are reasonably well reproduced by MCHIT using both G4BIC and G4QMD models. One can note a better agreement between the measured (Nakane & Sakamoto 2001) $yd(y)$ distributions and MCHIT calculations as compared with the PHITS code used for modeling (Tsuda et al. 2007) the same TEPC measurements (Nakane & Sakamoto 2001). This can be explained by the fact that in those PHITS calculations (Tsuda et al. 2007) the production and transport of δ -electrons was neglected, while these processes are taken into account in our MCHIT simulations.

6. TEPC response to a therapeutic ^{12}C beam

Now we turn to the central part of our study where we use MCHIT to model the response of the TEPC to a pencil-like therapeutic ^{12}C beam. We start with calculating the numbers of particles which traverse the TEPC placed at various positions in a water phantom and then continue with the distributions of the total track length inside the TEPC and with microdosimetry spectra.

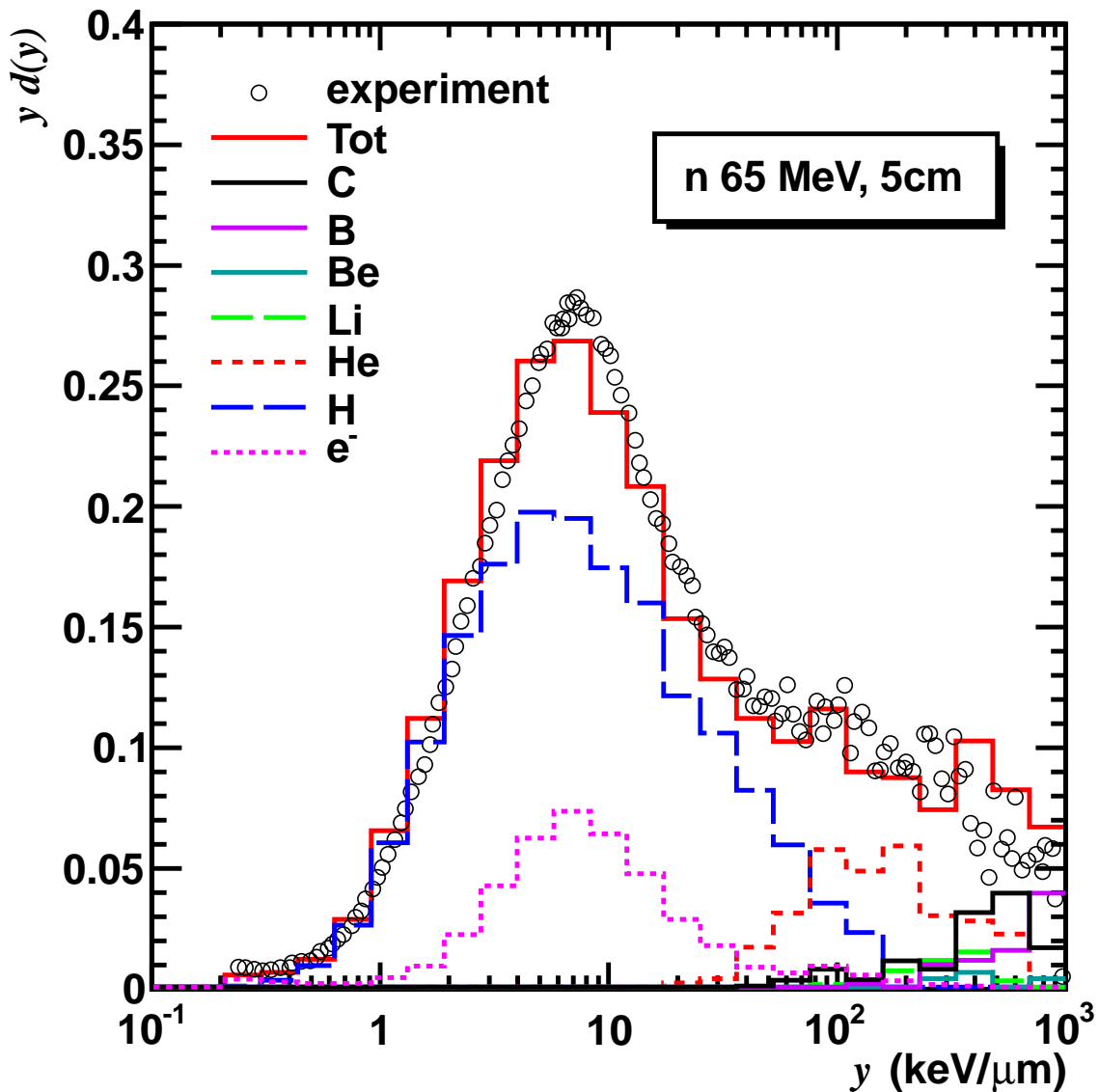


Figure 2. Calculated microdosimetric spectra for a TEPC at 5 cm depth inside a PMMA phantom irradiated by quasi-monoenergetic “65 MeV” neutrons. Results of MCHIT calculations with G4BIC model are shown. In addition to the total $yd(y)$ distribution the contributions of specific particles are shown by various histograms as explained on the legend. Experimental data (Nakane & Sakamoto 2001) are shown by points.

6.1. Number of particles which cross the TEPC

As described above in section 2, the lineal energy of a particle traversing a spherical TEPC can be estimated by dividing the energy ϵ imparted to the detector by the mean chord length $\bar{l} = 2/3d$, where d is the TEPC diameter. This estimation is based on the assumption that the TEPC is placed in a homogeneous radiation field and traversed by a single particle per event. This corresponds to the simplest standard event topology

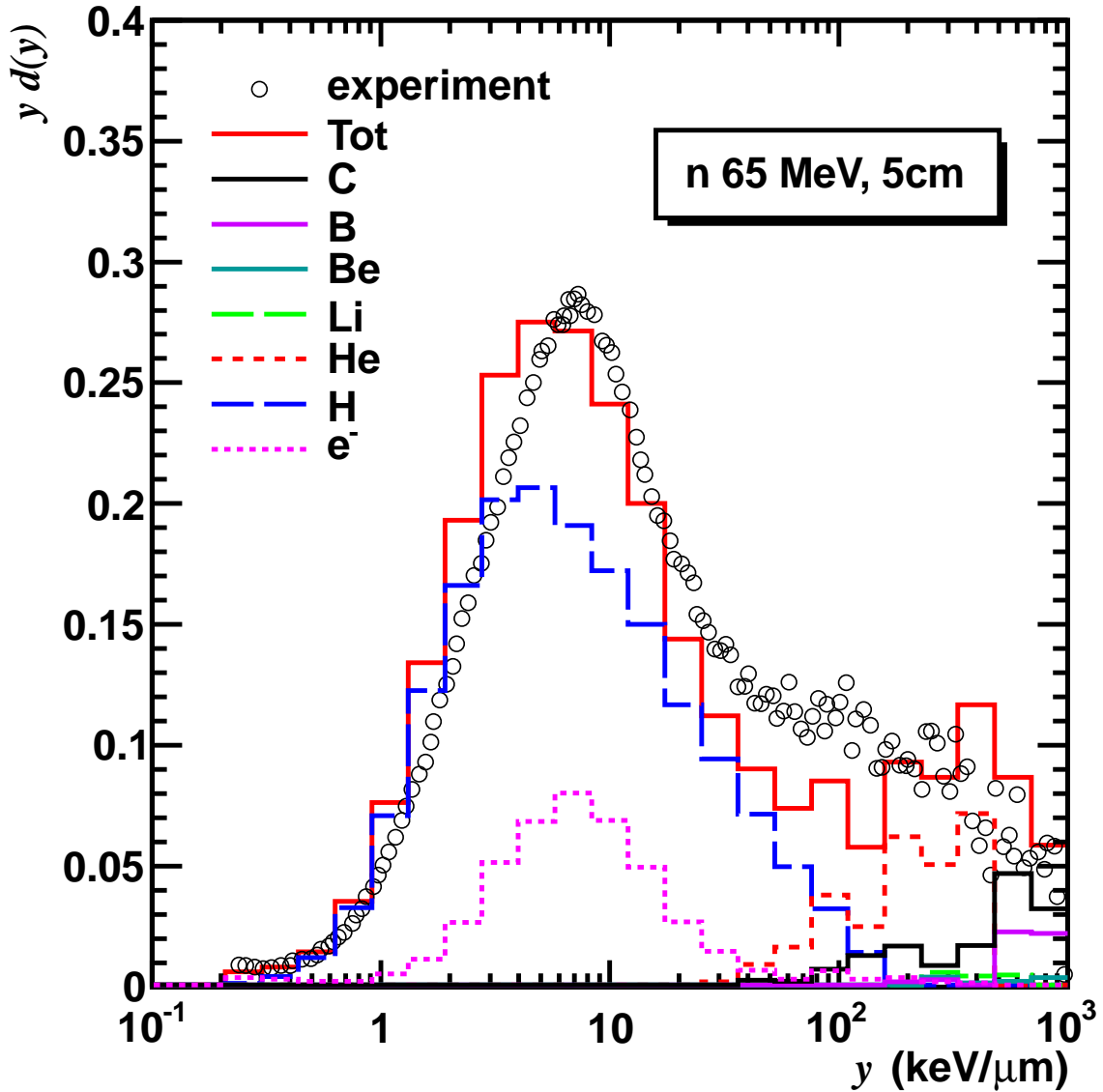


Figure 3. Same as in figure 2, but for MCHIT results with G4QMD model.

characterized by a single track with $l \leq d$. This means that the particle traverses the TEPC sensitive volume by a straight-line trajectory, it is not stopped inside the volume, and secondary particles are not produced neither in the volume nor in the vicinity of it.

In the experiment (Martino et al. 2010) the TEPC was irradiated either directly by a focused ^{12}C beam, or hit only by secondary particles at TEPC locations outside the beam spot. In this section we investigate the event topology relevant to the both cases. Indeed, on the contrary to the measurements with neutron beams described in section 5, the size of the ^{12}C beam was essentially smaller (3 mm FWHM) compared to the diameter of the TEPC sensitive volume ($d = 12.7$ mm). Therefore, for a TEPC placed on the beam axis at the plateau region of the depth-dose distribution and, possibly, close to the Bragg peak, the mean chord length will be larger than $2/3d$ due

to mostly central beam incidence. Moreover, several secondary particles can impact the TEPC in a single event. In this section we investigate whether the irradiation conditions match the standard ones for which the mean chord length $2/3d$ was used to calculate lineal energy y for a single particle traversal.

Since a TEPC detector is only sensitive to the total energy ϵ deposited to its volume given by the number of ionized atom-electron pairs produced in the gas chamber, the number of tracks in each event and their length (event topology) can not be identified in experiment. However, one can retrieve this information from MCHIT simulations by scoring the number of tracks and their total length inside the TEPCs. The probability distributions for the number of tracks $f(N)$ inside the TEPCs are shown in figure 4. The distributions are calculated for the events with at least one particle traversing the TEPC, and they are given at nine positions in the water phantom listed in table 2. These distributions are calculated per single beam particle and represent the probability for a TEPC placed at a certain position in the phantom to be traversed by N particles of any kind, where $N = 1$ corresponds to the standard event topology defined above despite of multiple δ -electrons stopped inside the TEPC. The tracks of the particles which do not deposit energy to the TEPC are also included.

The distributions presented in figure 4 were calculated with and without production of δ -electrons using the standard electromagnetic models. In the latter case only secondary nucleons and nuclear fragments were produced and counted while they traversed TEPCs. As one can see from the distribution calculated at “0 cm, plateau”, the TEPC at this location is traversed by beam particles with ~ 0.85 probability. This reflects the attenuation of the primary beam in the first 5 cm of water. On the contrary, the probability to hit the TEPC at “10 cm, tail” position far from the beam axis is only ~ 0.0053 per beam particle. As deduced from the comparison of the distributions calculated with and without generating δ -electrons, all TEPCs placed at the beam axis are usually traversed by several electrons in addition to nucleons and nuclei.

The topology of each event associated with the traversing of TEPC by one or several particles, can be characterized by the average number of tracks \bar{N} calculated per event. These average numbers are presented in each panel of figure 4 for both calculational options – with and without δ -electrons. When the production of δ -electrons is neglected, the most probable events are characterized by a single particle track, with $\bar{N} = 1.5$ and 1.4 under the direct impact of the beam at the plateau and peak, respectively. However, when the production of δ -electrons is considered, $\bar{N} = 3.6$ at the plateau and $\bar{N} = 2.7$ at the Bragg peak position. Although these electrons deliver less energy to the TEPC when compared to beam nuclei, their contribution can affect the results of simulations. As demonstrated in figure 4, the N -distributions and \bar{N} calculated for other seven positions are less affected by neglecting δ -electrons. At these positions the TEPCs are not directly impacted by the ^{12}C beam. When a lower energy threshold of 100 eV is used with the Penelope models, the average number of tracks on the beam axis is increased at the plateau to 3.7 and the Bragg peak position to 3.1, but for all other positions \bar{N} does not change.

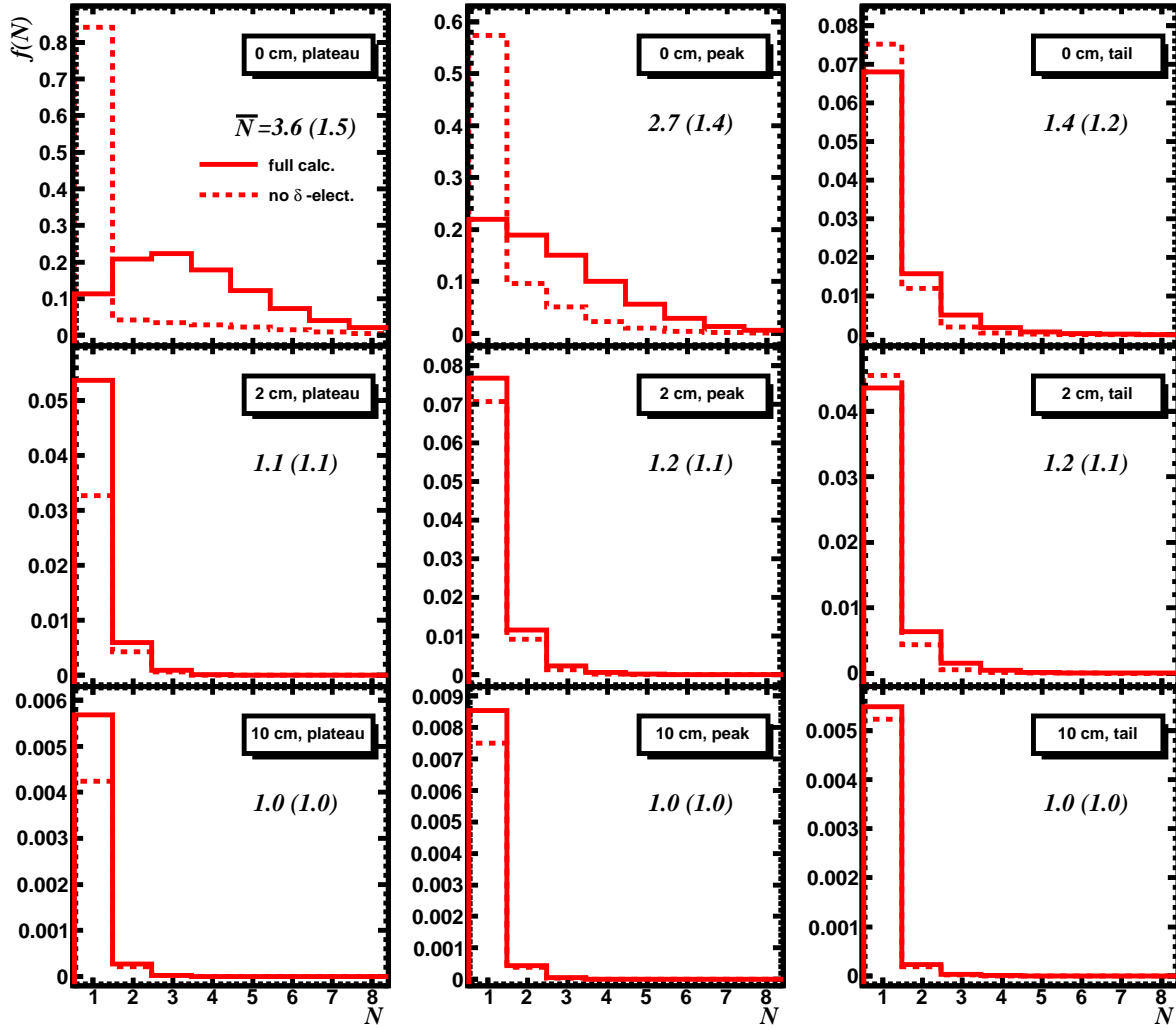


Figure 4. Probability distributions for the number of tracks in TEPCs at different locations in the water phantom irradiated by 300A MeV ^{12}C beam. The condition to have at least one track in the corresponding TEPC is applied. The distributions with and without simulation of δ -electrons are presented by solid- and dashed-line histograms, respectively, and calculated per beam particle. The average number of tracks \bar{N} per traversing event are presented for each TEPC location, and the values obtained without δ -electrons are given in parentheses.

The probability distributions $f(l)$ for the total track length l calculated with *G4PSPassageTrackLength* for particles traversing the TEPC at different locations in the water phantom are shown in figure 5. The values of \bar{l}/d calculated per event of TEPC traversing are also given for each TEPC position. The irradiation of TEPCs by a thin ^{12}C beam is clearly reflected in the $f(l)$ -distributions calculated for “0 cm, plateau” and “0 cm, peak”. As one can note, these distributions present a pronounced peak at the track length corresponding to the diameter of the gas cavity and a broad tail for higher track lengths with \bar{l}/d much larger than $2/3d$ due to secondary electrons and beam fragments. These distributions contrast to the linear dependence of $f(l)$

versus l (for $l < d$) found at all other TEPC positions which indicates a random particle incidence in the cavity. At “0 cm, tail” \bar{l}/d is still large, $\bar{l}/d \sim 0.936$, due to multiple tracks in a single event. Some events with two and three nucleons or nuclei in the TEPC are characterized by $l > d$ at “0 cm” positions, as already demonstrated earlier in figure 4. The distributions at the radius of 2 cm still exhibit the presence of one and two tracks of nucleons or nuclei in the TEPC. The mean chord length is close to $2/3d$ only for the TEPCs at the radius 10 cm. There the probability of an event with two particles in the TEPC is negligible.

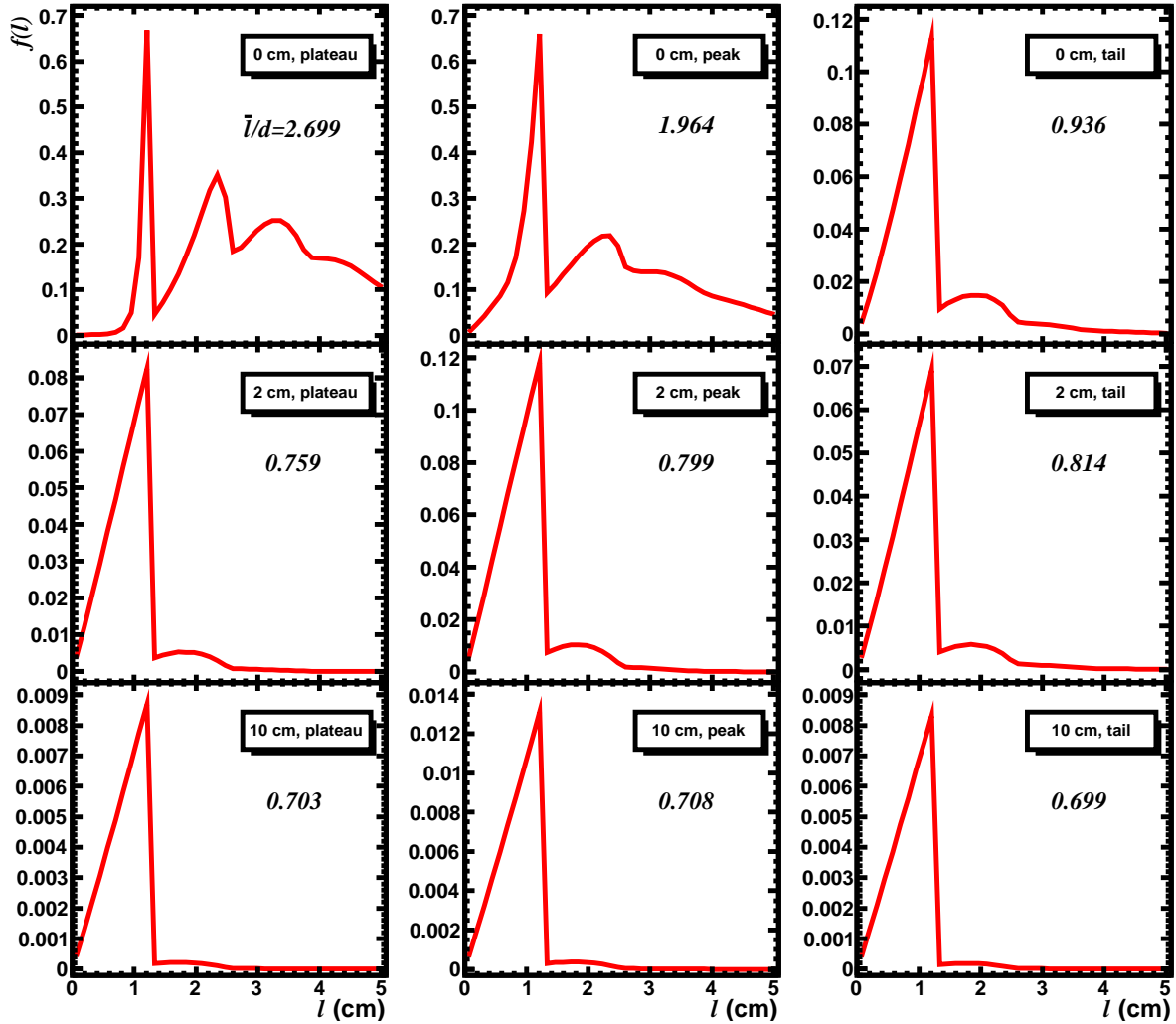


Figure 5. Probability distributions for the total track length for particles traversing the TEPCs at different locations in the water phantom irradiated by 300A MeV ^{12}C beam. The condition to have at least one track in the TEPC is applied. The calculations were performed with production of δ -electrons using the standard electromagnetic models. The average values of \bar{l}/d calculated per event are listed for each TEPC position.

The analysis of $f(N)$ and $f(l)$ distributions given in this section demonstrates different topologies of events in the TEPCs placed at the beam axis and far from the

beam. In the latter case the events are mostly characterized by the simplest standard topology associated with a single track of nucleon or nuclear fragment traversing the TEPC sensitive volume. On the contrary, the events in the TEPCs placed on the beam axis at the entrance to the phantom (“0 cm, plateau”) and at the Bragg peak (“0 cm, peak”) are more complicated. A part of events is characterized by one or two tracks of beam nuclei, secondary nucleons and/or nuclear fragments traversing the TEPC sensitive volume. In addition, tracks of two, three or more energetic electrons are frequently present in the TEPCs placed on the beam axis.

6.2. Lineal energy spectra inside the water phantom

Following the consideration given above to the particle track patterns in TEPCs, in figures 6 and 7 we present calculated microdosimetric $yd(y)$ distributions. The experimental data (Martino et al. 2010) were reported only above 0.3–0.5 keV/ μm . This range was also used to plot calculated microdosimetry spectra and calculate \bar{y}_f , \bar{y}_d in order to facilitate the comparison with the experimental data. As discussed in section 6.1, for the TEPCs placed on the beam axis, $\bar{l} > 2/3d$ since a certain number of events is characterized by more than one track traversing the TEPC, and events with small impact parameter are more frequent. However, in GSI measurements (Martino et al. 2010) $\bar{l} = 2/3d$ was assumed following the standard microdosimetry technique (International Commission of Radiation Units and Measurements (ICRU) 1983). The same normalization was taken in our calculations of y for the sake of a direct comparison with GSI data.

The MCHIT calculations were performed with different energy threshold for production of delta-electrons (with no production of delta-electrons taken as a limit case), and also with two different nuclear fragmentation models. The sensitivity of calculated distributions to computational parameters can be studied by comparing these distributions with each other and with experimental data.

The microdosimetric $yd(y)$ distributions measured at GSI (Martino et al. 2010) inside the water phantom irradiated by a 300A MeV ^{12}C beam are shown in figure 6 together with our simulation results. The distributions are given per beam particle for the same TEPC positions inside and outside the beam spot as listed in table 2 and described in section 6.1.

The influence of the energy threshold for production and transport of δ -electrons can be estimated by considering $yd(y)$ distributions obtained with and without simulating electron production, but with the same nuclear fragmentation model (G4QMD), as shown in figure 6. Here, the distributions calculated with these two options noticeably differ at the “0 cm, plateau” TEPC position close to the beam entrance to the phantom. In particular, the number of energy deposition events with $20 < y < 200$ keV/ μm is much higher compared to the calculation with δ -electrons. At this point fast beam nuclei produce energetic electrons which may escape from the TEPC sensitive volume and thus reduce the energy deposited to this volume. However, the $yd(y)$ distribution calculated

at the Bragg peak (at “0 cm, peak”) is not affected by neglecting δ -electrons. Much more secondary electrons are produced close to the Bragg peak, but they are generally less energetic compared to those at “0 cm, plateau” and do not escape from the TEPC. This means that the energy deposited to the TEPC at “0 cm, peak” can be simply calculated from the stopping power of beam nuclei even without modeling δ -electrons. As seen from figure 6, the production of δ -electrons also changes the distributions in

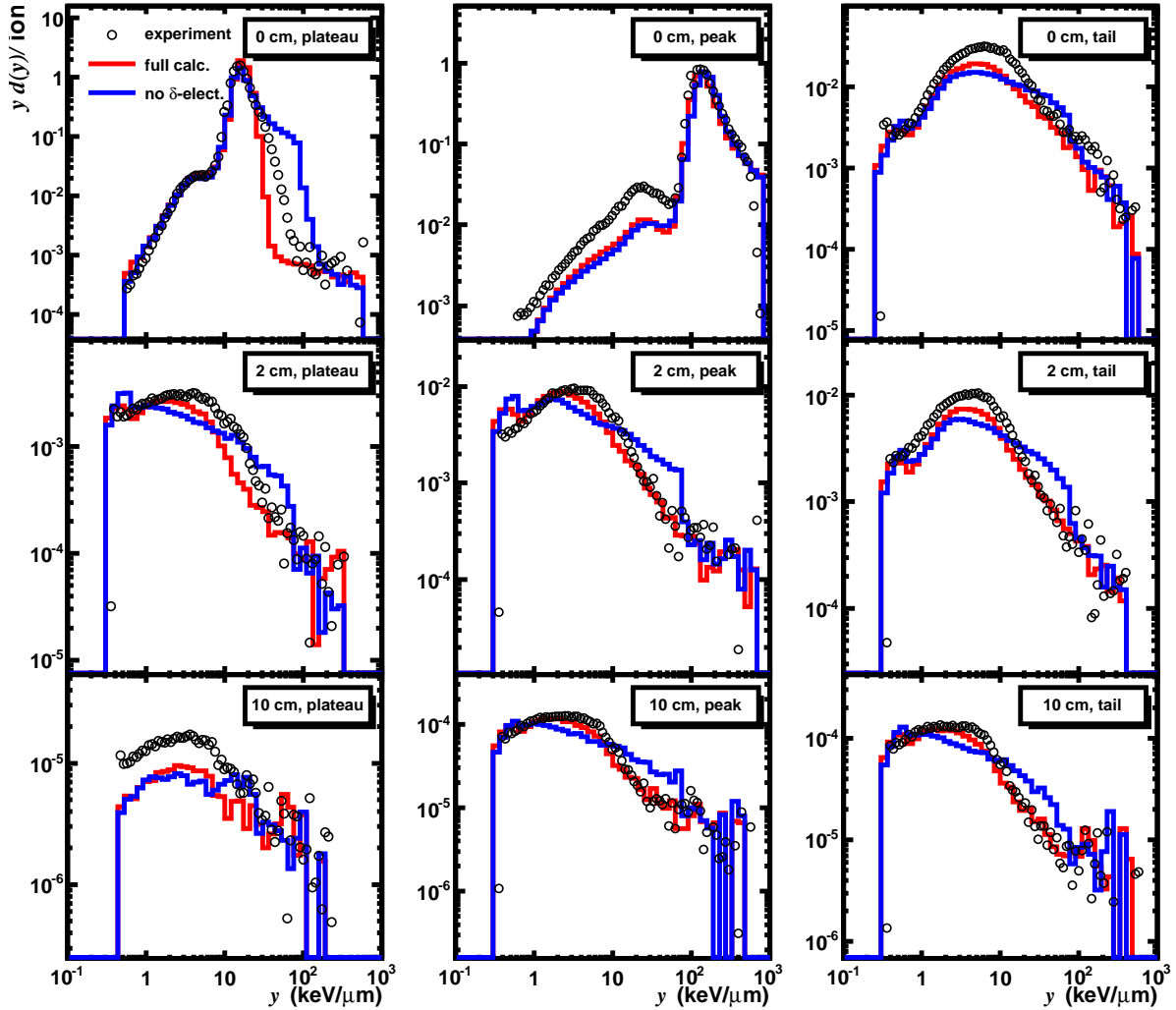


Figure 6. Microdosimetric $yd(y)$ distributions in water phantom irradiated by 300A MeV ^{12}C nuclei. Distributions calculated by MCHIT per beam particle with and without simulating δ -electrons are presented by red- and blue-line histograms, respectively. Points represent experimental data (Martino et al. 2010).

the range of $10 < y < 100 \text{ keV}/\mu\text{m}$ for the TEPCs located at 2 cm from the beam axis. Similar, but smaller changes in $yd(y)$ distributions associated with electron production are also found at 10 cm radii. At all these positions energy is deposited to the TEPC mostly by protons, and their contribution is reduced if secondary electrons are produced and escape the TEPC volume. The $yd(y)$ distributions with production and transport

of δ -electrons are not sensitive to a change in the lowest energy threshold from 990 eV to 100 eV with Penelope models.

MCHIT results obtained with G4BIC and G4QMD models used to simulate nuclear fragmentation are presented in figure 7 together with experimental data (Martino et al. 2010). One has to keep in mind the range of magnitudes of the distributions presented in nine panels of figures 6 and 7. They are normalized per single beam particle and have a span of almost six orders of magnitude. This is because of the fact that TEPC hits at the position “10 cm, plateau” are approximately 10^4 times less frequent than at the Bragg peak (“0 cm, peak”), as described below in section 6.3. The TEPCs located at 10 cm distance from the beam axis are hit exclusively by secondary particles (mostly nucleons) produced in nuclear fragmentation reactions. Therefore, the microdosimetry data (Martino et al. 2010) provide another possibility to validate the nuclear fragmentation models of Geant4.

Detailed consideration of the contributions of different charged particles to the calculated microdosimetric spectra will be given elsewhere (Burigo et al. 2013). In this work only general features of $yd(y)$ distributions are discussed, and the attention is focused on their general shape due to primary nuclei or secondary particles.

In the measurements (Martino et al. 2010) a sharp peak in the spectrum is observed at the TEPC position “0 cm, plateau”, figure 7. It is located at $y \sim 16 \text{ keV}/\mu\text{m}$, and its position is well reproduced by the MCHIT simulations with both G4BIC and G4QMD. However, as seen from the corresponding panel of figure 7, MCHIT predicts a slightly sharper drop of $yd(y)$ at the right slope of the peak. This peak is due to energetic beam nuclei that traverse the TEPC at the entrance to the phantom. As discussed in section 6.1, because of a relatively small beam diameter (3 mm FWHM) compared to the TEPC size, carbon nuclei propagate close to the diameter of the TEPC. As seen in the panel “0 cm, peak”, the peak in the $yd(y)$ distribution corresponding to ^{12}C nuclei becomes higher and broader as the TEPC is moved to the stopping point of beam nuclei. Compared to the “0 cm, plateau” panel, here the peak is shifted to a much higher value of $y \sim 131 \text{ keV}/\mu\text{m}$, and it has a prominent satellite peak with a maximum at $y \sim 25 \text{ keV}/\mu\text{m}$. The positions of both peaks are well reproduced by simulations. The observed shift of the main peak to larger y is due to increasing the LET of beam nuclei as they are slowing down with their penetration in water.

A common feature of the “0 cm, plateau” and “0 cm, peak” distributions consists in the presence of additional peaks at lower y values compared to the peaks of beam nuclei. Such satellite peaks are present due to relatively heavy projectile fragments (boron, beryllium and lithium nuclei) propagating with velocities close to the velocity of beam nuclei. Since their Z^2 are smaller, their ionization energy loss is reduced accordingly. This leads to reduced LET of secondary fragments compared to beam nuclei. While the satellite peak is accurately reproduced by theory at the entrance to the phantom at “0 cm, plateau”, a similar peak at “0 cm, peak” TEPC position is underestimated. This indicates, that the yields of secondary fragments are underestimated by the nuclear fragmentation models used in MCHIT.

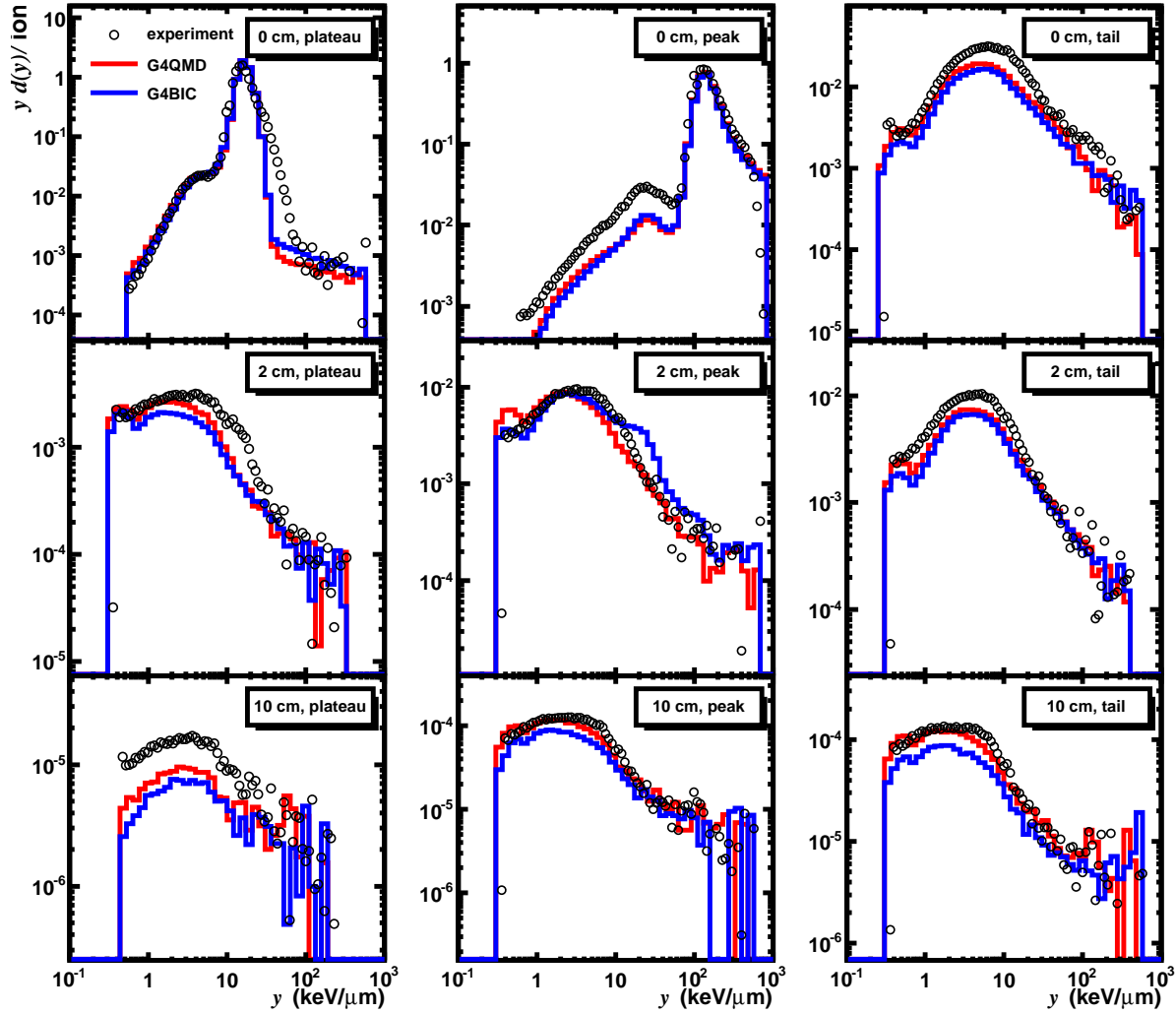


Figure 7. Microdosimetry spectra in water phantom irradiated by 300A MeV ^{12}C nuclei calculated by MCHIT with standard electromagnetic models including production and transport of δ -electrons and G4QMD and G4BIC options for nuclear fragmentation, shown as red- and blue-line histograms, respectively. Points represent experimental data (Martino et al. 2010).

The spectrum at the beam axis beyond the Bragg peak (“0 cm, tail”) and all the six spectra at 2 and 10 cm radii do not demonstrate any sharp peaks. This is because of contributions from various secondary light particles characterized by a broad range of kinetic energies and charges. It is expected that recoil charged particles produced in neutron-induced reactions also contribute to these spectra. This contribution is estimated below in section 7. While the general trends of the distributions measured at these seven points are reproduced by MCHIT, the absolute values are underestimated by a factor of two or slightly less. In view of a 10^4 difference in magnitude between “0 cm, tail” and “10 cm, plateau” distributions, such level of agreement between MCHIT and data can be accepted. Nevertheless, this discrepancy suggests that there is still a

room for improvements of the considered nucleus-nucleus collision models of Geant4, G4BIC and G4QMD, or de-excitation models.

6.3. Hit probability, \bar{y}_f , \bar{y}_d and dose inside the water phantom

We consider now the average microdosimetric quantities \bar{y}_f , \bar{y}_d defined in section 2 as well as the total dose at various positions inside the water phantom irradiated by 300A MeV ^{12}C nuclei. The total dose calculated at various distances from the beam axis is shown in figure 8 as a function of the depth in water together with measured dose values (Martino et al. 2010).

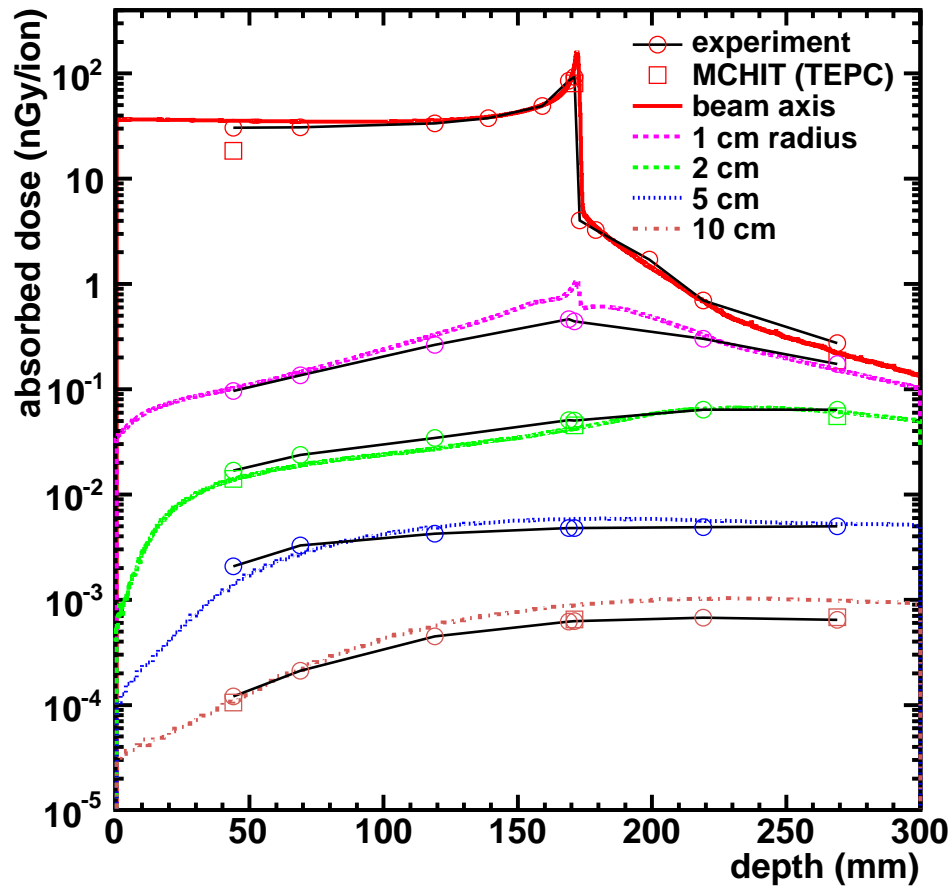


Figure 8. Calculated and measured total doses at various depths in the water phantom irradiated by 300A MeV ^{12}C nuclei. The doses calculated at 0, 2 and 10 cm radii from microdosimetry spectra by means of equation (3) are shown by open squares. Lines of various styles explained on the legend present total dose calculated in water by direct scoring of energy deposition at 0, 1, 2, 5 and 10 cm radii. The measured doses (Martino et al. 2010) are shown by open circles connected by dark solid lines to guide the eye.

As explained by the legend of figure 8, calculated doses were obtained by two different methods. In the first method labeled as “MCHIT (TEPC)” the dose delivered to the tissue-equivalent gas was computed from microdosimetry spectra by calculating firstly \bar{y}_f and then dose according to equation (3). In the second method calculations

were performed in water without placing TEPC. In the latter method a set of concentric rings was defined inside the phantom with 0.1 mm steps in the depth and radius. At the end of each run the energy imparted to each ring was calculated and then divided by the mass of the ring and by the number of beam particles. Due to a finite size of the TEPC, particles traverse it at various distances from the beam axis. Therefore, in calculating the dose without TEPC one has to take an average dose value for a characteristic volume of a similar size. For example, the average dose for 0–6.35 mm radii was calculated to obtain the dose on the beam axis. The radial ring thickness for dose calculations was set to 2/3 of the TEPC diameter at other distances from the beam axis.

The calculated dose values obtained by MCHIT by explicit modeling of the TEPC agree well with the experimental data at most of the TEPC positions, see figure 8. However, the dose at “0 cm, plateau” is underestimated, as one could expect from microdosimetric spectrum calculated at this TEPC position where events in the range $25 < y < 80$ keV/ μm are underestimated, see figure 6. The dose values calculated in the water phantom without TEPC agree well with the TEPC-based measurements and TEPC-based simulations except the points in the vicinity of the Bragg peak. As expected, these points are characterized by high dose gradients which are predicted by calculations without TEPC, e.g. at 1 cm radius. These dose gradients are smoothed by taking average values in water over the above-described rings. However, the dose in TEPC-based measurements still differs from the dose calculated without TEPC in the Bragg peak region at 1 cm radius.

Figure 9 gives further insight into the influence of a finite size of TEPC on microdosimetry measurements with therapeutic pencil-like beams. The doses from TEPC-based simulations, calculations without TEPC and measured doses agree well with each other at 1 and 2 cm distance from the beam axis. The same is true for the measurements performed at the beam axis in the tail. In all these cases the spatial dose distribution is characterized by relatively small gradients inside TEPC volumes which suggests good agreement between calculations with and without TEPC. While a good agreement is observed between data and TEPC-based simulations, direct calculations of the dose differ from both of them on the beam axis at the plateau and peak. As seen, the local dose at the TEPC center is generally 2–3 times higher than the TEPC-measured and TEPC-simulated dose under the focused irradiation of this TEPC by 3 mm FWHM pencil-like beam. Our results suggest that a good agreement between measured and calculated doses can be obtained only by direct modeling of the TEPC geometry, and not by scoring the dose in simulations without TEPC, as done by other authors (Hultqvist et al. 2010, Taleei et al. 2011).

The calculated frequency-mean \bar{y}_f and dose-mean \bar{y}_d lineal energies are given in tables 3 and 4. The corresponding values calculated from experimental microdosimetric distributions are also given in these tables for comparison. In addition, the probability P_{TEPC} of energy deposition at a given TEPC position is also listed in table 3. From these probability values one can conclude, for example, that on average there is one deposition event per ~ 3000 beam particles for the TEPCs placed 10 cm away from

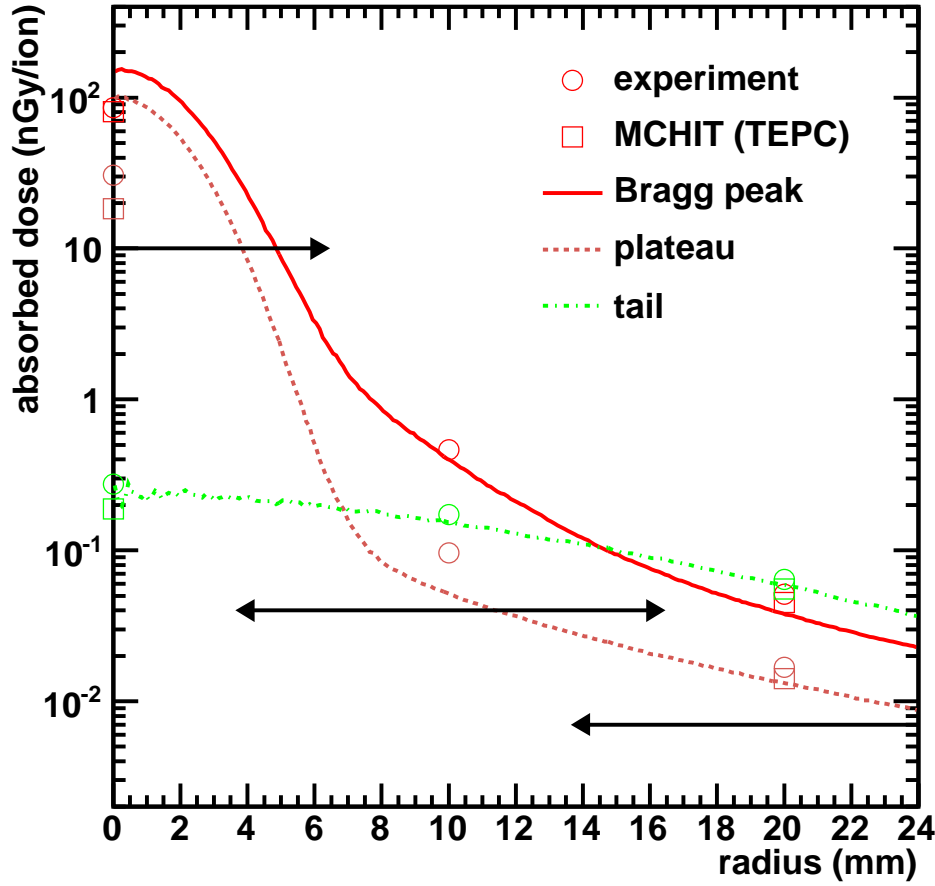


Figure 9. Calculated and measured total dose in the water phantom irradiated by 300A MeV ^{12}C nuclei as a function of the distance from the beam axis. The doses calculated on the beam axis and 20 mm away from it according to equation (3) are shown by open squares. Lines of various styles explained on the legend present total dose calculated in water by direct scoring of energy deposition at the plateau (44.04 mm depth), Bragg peak (171.04 mm) and tail (269.04 mm). The measured doses (Martino et al. 2010) are shown by open circles. Lines with arrows demonstrate the radial ranges covered by the TEPC placed at 0, 10 and 20 mm from the beam axis.

the beam axis, both at the peak and tail. The MCHIT results for \bar{y}_f obtained with the Penelope model are higher than those with the standard electromagnetic model by 1 – 10% depending on the TEPC position. The measured \bar{y}_f value on the beam axis at the plateau is well described by calculations while it is overestimated by $\sim 25\%$ at the peak. While calculated with Penelope model \bar{y}_f agree very well with \bar{y}_f measured at “2 cm, tail” and “10 cm, plateau” positions, the calculated \bar{y}_f are smaller compared to measured values by 10 – 20% at other four positions where TEPCs are mostly hit by secondary protons and neutrons.

The calculated and measured \bar{y}_d values are presented in table. 4. As seen from the table, \bar{y}_d calculated with the standard electromagnetic and Penelope models agree well with each other and with experimental data at the beam axis. The difference between calculated and measured values increases as the distance to the beam axis increases.

Table 3. Probabilities to deposit energy in the TEPC per beam particle at various positions inside the water phantom and the corresponding \bar{y}_f calculated per energy deposition event. The calculations were performed with Standard Electromagnetic Physics (Option 3) physics list. The results obtained with *G4EmPenelope* model for transporting electrons, positrons and gammas are given in the fourth column. The values of \bar{y}_f calculated from experimental (Martino et al. 2010) distributions $yd(y)$ are given for comparison.

TEPC's position	P_{TEPC}	\bar{y}_f (keV/ μm)	\bar{y}_f (keV/ μm)	\bar{y}_f (keV/ μm)
	MCHIT	MCHIT	MCHIT	GSI experiment
	Standard opt3	Standard opt3	Penelope	
0 cm, plateau	$9.87 \cdot 10^{-1}$	14.8	15.2	15.1
0 cm, peak	$6.44 \cdot 10^{-1}$	97.4	99.2	78.7
0 cm, tail	$5.10 \cdot 10^{-2}$	2.89	3.27	3.52
2 cm, plateau	$8.25 \cdot 10^{-3}$	1.24	1.34	1.69
2 cm, peak	$2.43 \cdot 10^{-2}$	1.39	1.54	2.01
2 cm, tail	$2.01 \cdot 10^{-2}$	2.13	2.36	2.41
10 cm, plateau	$3.19 \cdot 10^{-5}$	2.21	2.18	2.13
10 cm, peak	$3.62 \cdot 10^{-4}$	1.33	1.48	1.65
10 cm, tail	$3.87 \cdot 10^{-4}$	1.31	1.40	1.59

As only protons and neutrons contribute for TEPC positions far from the beam, this discrepancy points at the necessity to improve the description of production of these secondary particles by MCHIT.

Table 4. Calculated and measured (Martino et al. 2010) \bar{y}_d per energy deposition event in each TEPC. The calculations were performed with Standard Electromagnetic Physics (Option 3) physics list. The results obtained with *G4EmPenelope* model for transporting electrons, positrons and gammas are given in the third column. The experimental values were obtained by integrating $yd(y)$ distributions normalized per event.

TEPC's position	\bar{y}_d (keV/ μm)	\bar{y}_d (keV/ μm)	\bar{y}_d (keV/ μm)
	MCHIT	MCHIT	GSI experiment
	Standard opt 3	Penelope	
0 cm, plateau	16.9	17.2	18.1
0 cm, peak	177.	181.	170.
0 cm, tail	13.3	13.7	14.3
2 cm, plateau	6.67	5.68	7.40
2 cm, peak	8.22	8.81	9.06
2 cm, tail	10.4	10.6	9.79
10 cm, plateau	14.7	12.5	13.5
10 cm, peak	11.5	16.8	10.6
10 cm, tail	11.3	15.0	9.25

6.4. Relations between \bar{y}_f and LET for various beam profiles and surrounding media

As discussed in section 6.1, the TEPC response to focused and homogeneous irradiation is different. It can be also influenced by the media which surrounds the TEPC, as particles produced in this media, e.g. in fragmentation reactions, also hit the detector. It is expected (International Commission of Radiation Units and Measurements (ICRU) 1983) that the relation:

$$\bar{y}_f = L , \quad (4)$$

should hold for a spherical TEPC randomly traversed by particles with a constant LET L , in the case when the production of δ -electrons and other secondary particles is neglected. The relations between measured, simulated \bar{y}_f and LET under various conditions can be assessed by considering table 5. In addition to \bar{y}_f calculated with default physics settings of MCHIT and labeled with (a); the results obtained with the Penelope model used for transporting electrons (b); without simulating the production and transport of δ -electrons (c); and without simulating nuclear reactions (d) are presented.

In table 5 the results for the TEPC placed at “0 cm, plateau” at the depth of 52.1 mm in water under the impact of 3 mm FWHM beam at the entrance of the phantom are presented, cases (1a), (1b), (1c) and (1d). At this TEPC position the energy of ^{12}C at the entrance to the TEPC volume is estimated as $\sim 218A$ MeV, and it is close to the beam energy (220A MeV) used by Taddei et al. for homogeneous irradiation of a similar TEPC, but surrounded by air (Taddei et al. 2008). The thickness of the TEPC wall was twice as large (2.54 mm) compared to the TEPC used at GSI, and their TEPC operated at different tissue-equivalent gas pressure (effective diameter of 3 μm). Furthermore, those energy deposition events in the TEPC due to outgoing nuclei different from the incoming beam nuclei were ruled out in the experimental method. All these details were taken into account in our simulations. The comparison of these various irradiation conditions is presented in table 5.

The \bar{y}_f of 14.8 keV/ μm calculated with MCHIT in the case (1a) for TEPC in water is quite close to the experimental result of GSI (15.1 keV/ μm) and LET (15.23 keV/ μm). In the case (1b) the Penelope model with the production and transport of δ -electrons extended to lower electron energy provides a larger \bar{y}_f , of 15.2 keV/ μm , due to the enhancement of energy deposition inside the gas cavity by low-energy δ -electrons produced in the plastic shell. In the case (1c) the production of δ -electrons is neglected in the calculation, and \bar{y}_f increases to 16.2 keV/ μm and exceeds the corresponding LET. This is because of additional energy deposition in the TEPC sensitive volume which otherwise would be taken away by secondary electrons propagating beyond the TEPC. The case (1d) presents calculations performed with taking into account secondary electrons, but neglecting beam fragmentation. This means that instead of the mixture of ^{12}C beam nuclei and secondary fragments, which hit the TEPC in the cases (1a), (1b) and (1c), the detector is traversed only by ^{12}C nuclei and due to their higher Z^2 factor, \bar{y}_f increases to 16.5 keV/ μm , well above the measured \bar{y}_f and also LET. This

Table 5. Calculated and measured frequency-mean lineal energy \bar{y}_f per energy deposition event in the TEPC. Results are given for a Gaussian-shape 3 mm FWHM beam profile (1,2) and for homogeneous irradiation of the TEPC (3) surrounded by water (1) or air (2,3). Calculations with various physics settings are marked by letters: (a) - default MCHIT physics, (b) - the Penelope model for electrons, (c) - without simulation of δ -electrons, (d) - without simulation of nuclear fragmentation. Experimental data (Martino et al. 2010), (1) and (Taddei et al. 2008), (3) are given for comparison with MCHIT results. LET values calculated (Toftagaard & Bassler 2012, Luhr et al. 2012) according to ICRU Report 73 (International Commission of Radiation Units and Measurements (ICRU) 2005) are also given.

case	beam energy (MeV/ nucleon)	beam profile	media	\bar{y}_f (keV/ μm)			LET (keV/ μm)
				Calculation		Experiment	
				MCHIT	Taddei et al.	Martino et al. Taddei et al.	
(1a)	218	Gaussian	water	14.8		15.1	15.23
(1b)	218	Gaussian	water	15.2		15.1	15.23
(1c)	218	Gaussian	water	16.2		15.1	15.23
(1d)	218	Gaussian	water	16.5		15.1	15.23
(2a)	220	central incidence	air	20.4			15.14
(3a,d)	220	flat	air	13.8	14.5	13.4	15.14
(3b,d)	220	flat	air	14.1	14.5	13.4	15.14

also explains the value of \bar{y}_f calculated for the conditions of the second experiment, but with central incidence of ^{12}C nuclei on TEPC, case (2a). There the beam fragmentation outside the TEPC is negligible as it is surrounded by air. Since in this case the TEPC is traversed exclusively by ^{12}C nuclei along the TEPC diameter, this explains the largest energy deposition, and hence the largest \bar{y}_f of 20.4 keV/ μm calculated for this case.

In order to demonstrate the dependence of \bar{y}_f on the beam shape, the case of a flat beam (3) was also considered. In this case $\bar{y}_f = 13.8$ keV/ μm . This is noticeably smaller than \bar{y}_f of the case (2a), 20.4 keV/ μm , calculated for the central-incidence of ^{12}C of the same energy. The ratio between \bar{y}_f for the random impact on the TEPC (3) and for the central beam incidence (2) is remarkably close to the expected value of 2/3. One can note that the MCHIT result for the flat beam is closer to the experimental value than the value calculated by Taddei et al. with another version (7.1) of the Geant4 toolkit. We attribute this improvement to the changes in electromagnetic models done since the release of the version 7.1 and to differences in calculational parameters. However, all calculated and measured \bar{y}_f for the flat beam are smaller by $\sim 10\%$ compared to LET.

Our results demonstrate that depending on the beam profile the measured \bar{y}_f are either $\sim 35\%$ higher than corresponding LET for central beam incidence, case (2a), or $\sim 10\%$ lower than LET for homogeneous irradiation, case (3). At the same time,

for the case of TEPC irradiation by the Gaussian-shape 3 mm FWHM beam typical for scanning-beam therapy facilities, which is an intermediate case with respect to (2a) and (3), the correspondence between calculated \bar{y}_f and LET is good. As follows from this analysis, the exact modeling of TEPC irradiation conditions (the beam profile and surrounding media) is crucial for reproducing experimental data.

7. Contributions of secondary neutrons to microdosimetric quantities

The assignment of energy-dependent weighting factors is crucial for calculating equivalent doses for neutrons, e.g. in radiation protection. As discussed in several publications, the calculations of dose from secondary neutrons in proton (Jiang et al. 2005, Jarlskog & Paganetti 2008, Xu et al. 2008) and heavy-ion (Newhauser & Durante 2011) therapy are prone to various uncertainties. First, there are common difficulties for all kinds of radiation in estimating the risks from low doses (Kellerer 2000). Second, depending on the kind of tissue under irradiation *in vivo* and neutron energy, the relative biological efficiency (RBE) varies from 2 to 50 (Grahm et al. 1992) or even from 7 to 70 (Dennis 1987). Third, the fraction of neutrons in complex radiation fields surrounding therapeutic beams should be also properly evaluated, as discussed in this section.

The calculations presented above in section 5 demonstrate that fast neutrons deposit energy to the tissue-like media mostly by recoil protons. Neutrons produced in fragmentation reactions during particle therapy can travel long distances before they interact, thus depositing energy all over the patient's body. This issue was specially investigated with the MCHIT (Pshenichnov et al. 2005) with the conclusion that the neutron doses in carbon and proton therapy are at the same order, about 1% of the total dose. As demonstrated by recent measurements (Yonai et al. 2010), the dose from secondary neutrons in passive carbon-ion therapy is indeed comparable to the neutron dose in proton therapy. However, it is not yet clear whether neutrons produced during proton or carbon treatments essentially elevate the risk of secondary cancer (Jiang et al. 2005, Jarlskog & Paganetti 2008, Xu et al. 2008, Newhauser & Durante 2011). The contributions of secondary neutrons to the microdosimetric spectrum can be measured applying a veto counter technique which classify events due to charged or neutral particles. This technique was used elsewhere (Endo, Tanaka, Takada, Onizuka, Miyahara, Sato, Ishikawa, Maeda, Hayabuchi, Shizuma & Hoshi 2007, Wissmann et al. 2010) for 290A MeV carbon beam in acrylic phantom and 200A MeV carbon beam in water phantom, respectively. Endo et al. found that the neutron contribution to the deposited dose in the tail was 18% for the beam axis and 51% at 10 cm radius. For larger distances from the beam axis the neutron dose is predominant, increasing from 74% in forward direction to 89% in backward direction at 15 cm radius.

In GSI measurements (Martino et al. 2010) contributions to microdosimetric quantities from secondary neutrons were not identified. Monte Carlo simulations with MCHIT make it possible to estimate the energy deposition due to interactions of

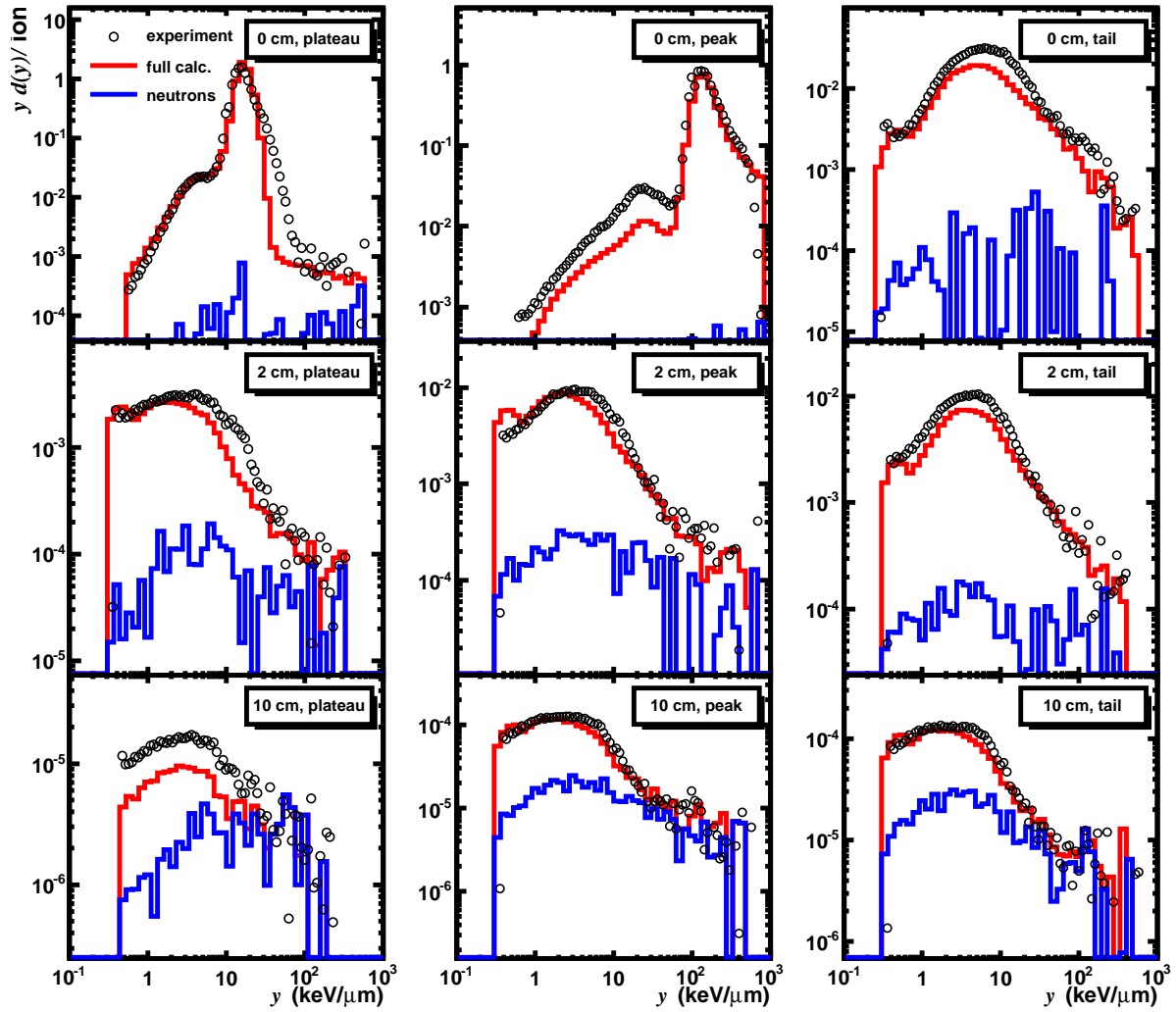


Figure 10. Microdosimetry spectra in water phantom irradiated by 300A MeV ^{12}C nuclei calculated with MCHIT. Simulations are performed with G4QMD model. Points represent experimental data (Martino et al. 2010).

neutrons. This is performed in two steps. Firstly, the energy deposition and lineal energy spectra are calculated taking into account all relevant physics processes, including production of secondary neutrons and their interactions with the phantom and TEPC. Secondly, calculations are performed for the same set-up including neutron production, but neglecting secondary interactions of neutrons. Thus, the difference between these two simulations provides the neutron contributions to the dose and $yd(y)$ distributions. The absolute dose and relative dose values from neutrons obtained by MCHIT following this procedure are given in table 6.

The contribution from secondary neutrons to the microdosimetric spectra is shown in figure 10. As seen, the relative neutron contribution increases with the distance from the beam axis. The neutron contribution at 10 cm radius increases from $\sim 25\%$ in the forward direction to $\sim 50\%$ in the backward direction. These results can not be directly

Table 6. Total dose, dose due to secondary neutrons and the relative neutron contribution to the dose in water phantom irradiated by 300A MeV ^{12}C pencil-like beam.

TEPC's position notation	Total Dose (nGy/ion)		Neutrons' Dose (MCHIT)	
	GSI experiment	MCHIT	(nGy/ion)	%
0 cm, plateau	30.6	18.4	$< 5.0 \cdot 10^{-3}$	< 0.03
0 cm, peak	93.4	80.6	$< 5.0 \cdot 10^{-2}$	< 0.06
0 cm, tail	$2.74 \cdot 10^{-1}$	$1.88 \cdot 10^{-1}$	$1.1 \cdot 10^{-3}$	0.6
2 cm, plateau	$1.68 \cdot 10^{-2}$	$1.41 \cdot 10^{-2}$	$7.8 \cdot 10^{-4}$	5.5
2 cm, peak	$5.04 \cdot 10^{-2}$	$4.52 \cdot 10^{-2}$	$2.0 \cdot 10^{-3}$	4.4
2 cm, tail	$6.42 \cdot 10^{-2}$	$5.56 \cdot 10^{-2}$	$1.6 \cdot 10^{-3}$	2.8
10 cm, plateau	$1.20 \cdot 10^{-4}$	$1.05 \cdot 10^{-4}$	$5.0 \cdot 10^{-5}$	47
10 cm, peak	$6.25 \cdot 10^{-4}$	$6.52 \cdot 10^{-4}$	$1.5 \cdot 10^{-4}$	23
10 cm, tail	$6.44 \cdot 10^{-4}$	$6.81 \cdot 10^{-4}$	$1.8 \cdot 10^{-4}$	26

compared to those of Endo et al. (Endo, Tanaka, Takada, Onizuka, Miyahara, Sato, Ishikawa, Maeda, Hayabuchi, Shizuma & Hoshi 2007) as they correspond to different TEPC position and beam profiles. However, the observed trend of increasing neutron contribution with respect to the distance from the primary beam is in agreement with their experimental findings. One should keep in mind, however, that the absolute doses are very small in these regions.

8. Conclusions

As stated in a well-known publication on microdosimetry (International Commission of Radiation Units and Measurements (ICRU) 1983), p 38: “Experiments and calculations of microdosimetric spectra play complementary roles. The degree of agreement between experiment and theory serves as a test of the validity of both.” Following this approach we extended the MCHIT model to calculations of microdosimetric quantities characterizing the radiation effects of accelerated nucleons and nuclei. The results of the calculations are compared with recent data (Martino et al. 2010) obtained with a therapeutic 300A MeV ^{12}C beam and with microdosimetry data collected with quasi-monoenergetic neutrons (Nakane & Sakamoto 2001). To the best of our knowledge the present study is the first one which uses the Geant4 toolkit for calculating microdosimetric quantities by a detailed modeling of TEPCs located in a phantom both inside and outside of a therapeutic ^{12}C beam. The in-field and out-of-field y -distributions are obtained in a consistent approach and the contributions of secondary neutrons to out-of-field doses are evaluated. Our computational methods can be useful to assess the biological effects of complex radiation fields from therapeutic ion beams, including effects of secondary neutrons produced in carbon-ion therapy (Newhauser & Durante 2011).

Since a TEPC placed in a water phantom irradiated by nuclear beam inevitably changes the amount of material which is traversed by particles, the radiation field

is distorted in the presence of the detector. The TEPC geometry was thoroughly implemented in the Monte Carlo simulations performed in this work with the MCHIT model. Realistic models from Geant4 toolkit were used to describe particles propagation and energy deposition in non-uniform medium. This allowed us to obtain a good agreement between calculated and measured microdosimetric quantities for different TEPC positions inside the water phantom irradiated by the pencil-like beam of 300A MeV ^{12}C nuclei. Our main conclusions are as follows:

- The MCHIT model is able to describe the spatial distribution of the total dose in the water phantom despite of six orders of magnitude decrease of dose with increasing distance from the beam axis.
- The contributions of delta-electrons on energy deposited to TEPC varies at different TEPC locations in the water phantom. The propagation of energetic beam nuclei through a TEPC is accompanied by production of energetic delta-electrons, which may escape the TEPC sensitive volume, thus reducing the deposited energy, while this effect is less important for the detectors impacted only by secondary nucleons, which produce low-energy electrons far from the beam axis.
- Contributions of primary beam nuclei and secondary fragments can be distinguished in the calculated and measured $yd(y)$ microdosimetric spectra on the beam axis.
- Proper modeling of nuclear fragmentation reactions is crucial for describing microdosimetric distributions both on the beam axis and far from the beam. The nuclear fragmentation models of Geant4, G4QMD and G4BIC, are equally suitable for describing general features of the spectra, but both underestimate the fluxes of protons and neutrons far from the beam. This indicates the necessity of improving nucleus-nucleus collision models in calculating the angular and energy distributions of secondary nucleons and nuclear fragments.
- The values of \bar{y}_f and \bar{y}_d for a TEPC under direct impact of projectile nuclei are sensitive to the beam profile.
- The MCHIT model describes well the $yd(y)$ distributions in the PMMA phantom irradiated by quasi-monoenergetic neutrons. This justifies the use of this model for calculating the TEPC response to secondary neutrons from ^{12}C beam.
- The contribution of secondary neutrons to the out-of-field dose from ^{12}C beams estimated from MCHIT simulations amounts to about 50% of the total far from the beam. Since experimental identification of neutrons would require bulky detectors placed only outside the water phantom, such microdosimetry measurements remain the only solution to estimate the upper limits for the dose from neutrons and their radiation quality close to the target volume.

Our results can be extended to other measurements with TEPC, in particular with other kinds of nuclear beams, as the TEPC model (Far West Technology Inc., LET-1/2) simulated in this work is used worldwide. A detailed consideration of contributions of specific nuclear fragments to $yd(y)$ distributions calculated with MCHIT will be given elsewhere (Burigo et al. 2013).

Acknowledgments

The presented results were obtained in the framework of NanoBIC-NanoL project. L.B. is grateful to the Beilstein Institute for support. This work was also partially supported by HIC for FAIR within the Hessian LOEWE-Initiative. We wish to thank D. Schardt, G. Martino, C. La Tessa and M. Durante for numerous discussions which inspired us to conduct this theoretical study and also for providing us with their tables of experimental data. Our calculations were performed at the Center for Scientific Computing (CSC) of the Goethe University Frankfurt. We are grateful to the staff of the Center for support.

References

- Agostinelli S, Allison J, Amako K, Apostolakis J, Araujo H, Arce P, Asai M, Axen D, Banerjee S, Barrand G, Behner F, Bellagamba L, Boudreau J, Broglia L, Brunengo A, Burkhardt H, Chauvie S, Chuma J, Chytracek R, Cooperman G, Cosmo G, Degtyarenko P, Dell'Acqua A, Depaola G, Dietrich D, Enami R, Feliciello A, Ferguson C, Fesefeldt H, Folger G, Foppiano F, Forti A, Garelli S, Giani S, Giannitrapani R, Gibin D, Cadenas J, Gonzalez I, Abril G, Greeniaus G, Greiner W, Grichine V, Grossheim A, Guatelli S, Gumplinger P, Hamatsu R, Hashimoto K, Hasui H, Heikkinen A, Howard A, Ivanchenko V, Johnson A, Jones F, Kallenbach J, Kanaya N, Kawabata M, Kawabata Y, Kawaguti M, Kelner S, Kent P, Kimura A, Kodama T, Kokoulin R, Kossov M, Kurashige H, Lamanna E, Lampen T, Lara V, Lefebure V, Lei F, Liendl M, Lockman W, Longo F, Magni S, Maire M, Medernach E, Minamimoto K, de Freitas P, Morita Y, Murakami K, Nagamatu M, Nartallo R, Nieminen P, Nishimura T, Ohtsubo K, Okamura M, O'Neale S, Oohata Y, Paech K, Perl J, Pfeiffer A, Pia M, Ranjard F, Rybin A, Sadilov S, Di Salvo E, Santin G, Sasaki T, Savvas N, Sawada Y, Scherer S, Seil S, Sirotenko V, Smith D, Starkov N, Stoecker H, Sulkimo J, Takahata M, Tanaka S, Tcherniaev E, Tehrani E, Tropeano M, Truscott P, Uno H, Urban L, Urban P, Verderi M, Walkden A, Wander W, Weber H, Wellisch J, Wenaus T, Williams D, Wright D, Yamada T, Yoshida H & Zschiesche D 2003 *Nucl. Instrum. Methods A* **506**(3), 250–303.
- Allison J, Amako K, Apostolakis J, Araujo H, Dubois P, Asai M, Barrand G, Capra R, Chauvie S, Chytracek R, Cirrone G, Cooperman G, Cosmo G, Cuttone G, Daquino G, Donszelmann M, Dressel M, Folger G, Foppiano F, Generowicz J, Grichine V, Guatelli S, Gumplinger P, Heikkinen A, Hrivnacova I, Howard A, Incerti S, Ivanchenko V, Johnson T, Jones F, Koi T, Kokoulin R, Kossov M, Kurashige H, Lara V, Larsson S, Lei F, Link O, Longo F, Maire M, Mantero A, Mascialino B, McLaren I, Lorenzo P, Minamimoto K, Murakami K, Nieminen P, Pandola L, Parlati S, Peralta L, Perl J, Pfeiffer A, Pia M, Ribon A, Rodrigues P, Russo G, Sadilov S, Santin G, Sasaki T, Smith D, Starkov N, Tanaka S, Tcherniaev E, Tome B, Trindade A, Truscott P, Urban L, Verderi M, Walkden A, Wellisch J, Williams D, Wright D & Yoshida H 2006 *IEEE T. Nucl. Sci.* **53**(1, Part 2), 270–278.
- Böhlen T T, Cerutti F, Dosanjh M, Ferrari A, Gudowska I, Mairani A & Quesada J M 2010 *Phys. Med. Biol.* **55**(19), 5833–5847.
- Böhlen T T, Dosanjh M, Ferrari A & Gudowska I 2012 *Int. J. Radiat. Biol.* **88**(1-2), 176–182.
- Böhlen T T, Dosanjh M, Ferrari A, Gudowska I & Mairani A 2011 *Phys. Med. Biol.* **56**, 6545–6561.
- Bondorf J, Botvina A, Iljinov A, Mishustin I & Sneppen K 1995 *Phys. Rep.* **257**(3), 133–221.
- Burigo L, Pshenichnov I, Mishustin I & Bleicher M 2013. Manuscript in preparation.
- Dennis J 1987 *Progress in Nuclear Energy* **20**(2), 133–149.
- Durante M & Loeffler J S 2010 *Nat. Rev. Clin. Oncol.* **7**(1), 37–43.
- Elsaesser T, Weyrather W K, Friedrich T, Durante M, Iancu G, Kraemer M, Kragl G, Brons S, Winter M, Weber K J & Scholz M 2010 *Int. J. Radiat. Oncol.* **78**(4), 1177–1183.

- Endo S, Takada M, Onizuka Y, Tanaka K, Maeda N, Ishikawa M, Miyahara N, Hayabuchi N, Shizuma K & Hoshi M 2007 *J. Radiat. Res.* **48**(5), 397–406.
- Endo S, Takada M, Tanaka H, Onizuka Y, Tanaka K, Miyahara N, Baba H, Oishi A, Ishikawa M, Hoshi M, Kimura S, Minematsu M, Morimune Y, Kojima Y & Shizuma K 2010 *Radiat. Environ. Bioph.* **49**(3), 469–475.
- Endo S, Tanaka K, Ishikawa M, Hoshi M, Onizuka Y, Takada M, Yamaguchi H, Hayabuchi N, Maeda N & Shizuma K 2005 *Med. Phys.* **32**(12), 3843–3848.
- Endo S, Tanaka K, Takada M, Onizuka Y, Miyahara N, Sato T, Ishikawa M, Maeda N, Hayabuchi N, Shizuma K & Hoshi M 2007 *Med. Phys.* **34**(9), 3571–3578.
- Geant4 Physics Reference Manual* 2011.
URL: <http://geant4.web.cern.ch/geant4/support/userdocuments.shtml>
- Grahn D, Lombard L S & Carnes B A 1992 *Radiation Research* **129**(1), 19–36.
- Gudowska I, Sobolevsky N, Andreo P, Belkic D & Brahme A 2004 *Phys. Med. Biol.* **49**(10), 1933–1958.
- Guetersloh S, Borak T, Taddei P, Zeitlin C, Heilbronn L, Miller J, Murakami T & Iwata Y 2004 *Radiat. Res.* **161**(1), 64–71.
- Haettner E, Iwase H & Schardt D 2006 *Radiat. Prot. Dosim.* **122**(1-4), 485–487. 14th International Symposium on Microdosimetry, Venice, ITALY, NOV 13-18, 2005.
- Hultqvist M, Lillhok J E, Lindborg L, Gudowska I & Nikjoo H 2010 *Radiat. Meas.* **45**(10, SI), 1238–1241. 11th Neutron and Ion Dosimetry Symposium (NEUDOS-11), Cape Town, SOUTH AFRICA, OCT 12-16, 2009.
- International Commission of Radiation Units and Measurements (ICRU) 1983 *Microdosimetry Report No 36* (Bethesda, MD).
- International Commission of Radiation Units and Measurements (ICRU) 1993 *Stopping Powers and Ranges for Protons and Alpha Particles Report No 49* (Bethesda, MD).
- International Commission of Radiation Units and Measurements (ICRU) 2005 *Stopping of Ions Heavier than Helium Report 73* (Oxford University Press).
- Jarlskog C Z & Paganetti H 2008 *Int. J. Radiat. Oncol.* **72**(1), 228–235.
- Jiang H, Wang B, Xu X, Suit H & Paganetti H 2005 *Phys. Med. Biol.* **50**(18), 4337–4353.
- Kase Y, Kanai T, Matsumoto Y, Furusawa Y, Okamoto H, Asaba T, Sakama M & Shinoda H 2006 *Radiat. Res.* **166**(4), 629–638.
- Kase Y, Kanai T, Sakama M, Tameshige Y, Himukai T, Nose H & Matsufuji N 2011 *J. Radiat. Res.* **52**(1), 59–68.
- Kellerer A 2000 *Radiat. Environ. Bioph.* **39**(1), 17–24.
- Koi T 2010 *Proceedings of the MC2010 Monte Carlo Conference*.
- Kraemer M & Durante M 2010 *Eur. Phys. J. D* **60**(1), 195–202.
- Lechner A, Ivanchenko V N & Knobloch J 2010 *Nucl. Instrum. Methods B* **268**(14), 2343–2354.
- Lindborg L & Nikjoo H 2011 *Radiat. Prot. Dosim.* **143**(2-4), 402–408. 15th International Symposium on Microdosimetry, Verona, ITALY, OCT 25-30, 2009.
- Luhr A, Toftegaard J, Kantemiris I, Hansen D C & Bassler N 2012 *Int. J. Radiat. Biol.* **88**(1-2), 209–212.
- Martino G, Durante M & Schardt D 2010 *Phys. Med. Biol.* **55**(12), 3441–3449.
- Mishustin I, Pshenichnov I & Greiner W 2010 *Eur. Phys. J. D* **60**(1), 109–114.
- Nakane Y & Sakamoto Y 2001 *Nucl. Instrum. Methods A* **459**(3), 552–564.
- Newhauser W D & Durante M 2011 *Nat. Rev. Cancer* **11**(6), 438–448.
- Nikjoo H, Khvostunov I K & Cucinotta F A 2002 *Radiat. Res.* **157**, 435–445.
- Pshenichnov I, Botvina A, Mishustin I & Greiner W 2010 *Nucl. Instrum. Methods B* **268**(6), 604–615.
- Pshenichnov I, Larionov A, Mishustin I & Greiner W 2007 *Phys. Med. Biol.* **52**(24), 7295–7312.
- Pshenichnov I, Mishustin I & Greiner W 2005 *Phys. Med. Biol.* **50**(23), 5493–5507.
- Pshenichnov I, Mishustin I & Greiner W 2006 *Phys. Med. Biol.* **51**(23), 6099–6112.
- Pshenichnov I, Mishustin I & Greiner W 2008 *Nucl. Instrum. Methods B* **266**(7), 1094–1098.
- Rossi H H 1990 *Radiat. Prot. Dosim.* **31**(1-4), 361–365. 10TH SYMP ON MICRODOSIMETRY,

ROME, ITALY, MAY 21-26, 1989.

- Schardt D, Elsaesser T & Schulz-Ertner D 2010 *Rev. Mod. Phys.* **82**(1), 383–425.
- Taddei P J, Borak T B, Guetersloh S B, Gersey B B, Zeitlin C, Heilbronn L, Miller J, Murakami T & Iwata Y 2006 *Radiat. Meas.* **41**, 1227–1234.
- Taddei P J, Zhao Z & Borak T B 2008 *Radiat. Meas.* **43**(9-10), 1498–1505.
- Taleei R, Hultqvist M, Gudowska I & Nikjoo H 2011 *Int. J. Radiat. Biol.* . [Epub ahead of print].
- Tobias F, Durante M, Taucher-Scholz G & Jakob B 2010 *Mutat. Res.-Rev. Mutat.* **704**, 54–60.
- Toftegaard J & Bassler N 2012 ‘Stopping power of ions’.
- URL:** <http://dedx.au.dk/>
- Tsuda S, Nakane Y & Yamaguchi Y 2007 *Radiat. Prot. Dosim.* **126**(1-4), 174–177. 10th International Symposium on Neutron Dosimetry, Uppsala, SWEDEN, JUN 12-16, 2006.
- Tsuda S, Sato T, Takahashi F, Satoh D, Endo A, Sasaki S, Namito Y, Iwase H, Ban S & Takada M 2010 *Phys. Med. Biol.* **55**(17), 5089–5101.
- Waker A J 1995 *Radiat. Prot. Dosim.* **61**(4), 297–308.
- Waker A J 2006 *Radiat. Prot. Dosim.* **122**(1-4), 369–373.
- Wissmann F, Giesen U, Klages T, Schardt D, Martino G & Sunil C 2010 *Radiat. Environ. Bioph.* **49**, 331–336.
- Xu X G, Bednarz B & Paganetti H 2008 *Phys. Med. Biol.* **53**(13), R193–R241.
- Yonai S, Kase Y, Matsufuji N, Kanai T, Nishio T, Namba M & Yamashita W 2010 *Med. Phys.* **37**(8), 4046–4055.